

FLEXIBLE CRYSTALLINE SILICON SOLAR CELL

By

WEI ZHANG, B.ENG.(MCMMASTER UNIVERSITY)

A Thesis

Submitted to the School of Graduate Studies

in Partial Fulfilment of the Requirements

for the Degree

Master of Applied Science

McMaster University

©Copyright by Wei Zhang, January 2008

MASTER OF APPLIED SCIENCE (2008)
(Department of Engineering Physics)

McMaster University
Hamilton, Ontario

TITLE: Flexible Crystalline Silicon Solar Cell

AUTHOR: Wei Zhang, B.Eng.(McMaster University)

SUPERVISOR: Professor A.H.Kitai

NUMBER OF PAGES: xiii, 94

Abstract

A new type of flexible silicon solar cell has been fabricated by interconnecting solar cell die on a flexible substrate. The fabrication process is described in this thesis. The solar cell die were diced using two methods. One method was to dice a solar cell completely through. The other method was to dice a solar cell from its back partially and then cleave through. To study the effects of different dicing methods on the performance of solar cell die, storage delay time measurement was employed to determine the lifetime of excess electrons in the p region of the two types of solar cell die. A laser beam induced current (LBIC) scanning technique was employed to study the electrical performance of the two types of solar cell die. The carrier diffusion lengths of two types of solar cell die were also determined by traveling light spot diffusion length measurement.

The theoretical response of a solar cell was compared to experimental results at various incident light angles. OpticLab software was used to model the incident light angle and lens spacing dependence of solar cell performance.

Acknowledgements

I would like to express my sincere appreciation and gratitude to my supervisor Dr. Adrian Kitai from whom I have obtained so much priceless knowledge, experience, and opportunities during my study. I am grateful for his guidance and support in the past two years.

I wish to acknowledge Dr. Yingwei Xiang, Mr. Feng Chen, Mr. Bo Li, Mr. Avery Yuen, Dr. Peter Shi and Dr. Huijuan Bi for their helpful suggestions and discussions. I would like to extend my thanks to Dr. Doug Bruce, Mr. Graham Pearson, Ms. Doris Stevanovic, Dr. Jian Yang and Ms. Fangfang Zhang for their assistance in using equipments. I appreciate Mr. Wenhe Gong for his help with X-ray experiment of material characterization. Many thanks are due to Mr. Adam Weaver and Mr. Donny Cosic for their assistance in the summer 2006 and 2007.

Finally, I would like to express my most appreciation and love to my mother Jufang Xu and father Shuping Zhang for their support and understanding in my life.

To my parents

Table of Contents

Abstract	iii
Acknowledgements	iv
List of Figures	viii
List of Tables	xiii
Chapter 1 Introduction	1
1.1 Development of silicon solar cell	1
1.2 Flexible solar cell	8
1.2.1 Amorphous silicon solar cell	9
1.2.2 Organic solar cell	14
1.2.3 Flexible silicon solar cell in this thesis	14
1.2.4 Comparison of three types of flexible solar cell	16
Chapter 2 Theory	19
2.1 Basic concepts of solar cell	19
2.2 Diffusion length calculation from light beam induced current scanning	24
2.3 Short circuit current	26
2.4 Semiconductor transport equations	28
2.5 Storage delay time	33
Chapter 3 Discussion of Flexible Silicon Solar Cell	38
3.1 Performance	38

3.2	Fabrication of flexible solar cell in this thesis	42
Chapter 4 Experiment and Discussion		44
4.1	Analysis of efficiency loss due to dicing process	44
4.1.1	Crystal structure of the test solar cell	44
4.1.2	Storage delay time measurement	47
4.1.3	Light beam induced current scanning	56
4.1.4	Traveling light spot diffusion length measurement	68
4.1.5	Correlation of three experiments	74
4.2	Determination of angle dependence and lens spacing of solar cell performance	79
Chapter 5 Conclusion		87
Chapter 6 Future work		90
Bibliography		92

List of Figures

1.1	Evolution of silicon laboratory cell efficiency.	4
1.2	A cross section view of PESC	5
1.3	A schematic structure of back contact cell	7
1.4	PERL structure	8
1.5	A schematic diagram of a-Si solar cell	10
1.6	Structure for a triple junction a-Si solar cell. The material for each layer is labeled	12
1.7	A roll-to-roll operation for the deposition of a triple junction solar cell . .	12
1.8	Flexible solar cell	15
2.1	A schematic diagram of a typical solar cell structure	20
2.2	I-V characteristics and the output power of a solar cell	21
2.3	Equivalent circuit of an ideal solar cell	22
2.4	A schematic diagram of a focused light beam on the edge of a solar cell .	24
2.5	A schematic diagram of a one dimensional cross-section solar cell structure. d is the junction depth.	26
2.6	The amount of charge buildup in the differential volume $\partial x A$ is determined in three parts: the current passing through the volume, the E-H pairs generation rate in the volume and the E-H pairs recombination rate in the volume.	29

2.7	A schematic diagram of a one dimensional cross-section solar cell structure. $-w_p$ and w_n are the edges of depletion region. d is the junction depth. $-x_p$ and x_n are the edge surfaces of the p-n junction solar cell	30
2.8	A schematic diagram of experiment setup for storage delay time measurement. The diode symbol represents a solar cell in a dark condition	33
2.9	Current through the solar cell	34
2.10	Excess electron distribution in the p-region as a function of time during the transient	34
3.1	Front view of flexible silicon solar cell sample in this thesis	39
3.2	Backside view of flexible silicon solar cell sample in this thesis	39
3.3	IV scan for the flexible solar cell sample in a dark condition	40
3.4	IV curve of a flexible silicon solar cell measured under one sun condition	41
3.5	Performance of 14 solar cell die in the sample cell	41
4.1	X-ray diffraction pattern of the test solar cell. The peak at 29.5 degree does not correspond to a silicon peak. It may be due to a Si-Br compound since P^+ doping is employed at the rear of the cell. Standard powder patten for silicon is shown.	45
4.2	X-ray diffraction pattern of a monocrystalline silicon material with [100] crystal orientation. Standard powder patten for Si.	46
4.3	Grains of the test solar cell	47
4.4	A solar cell is diced through	48
4.5	A solar cell is partially diced and then cleaved through	49

4.6 A schematic diagram of storage charge delay time measurement setup 50

4.7 A plot of measurement of storage delay time from measured voltages at point A and B with respect to time for one sample cell 51

4.8 The excess electron lifetime of 29 cell die diced all the way through 53

4.9 The excess electron lifetime of 15 cells diced partially and then cleaved through 54

4.10 Two Gaussian distributions for two different diced sample data. The blue curve represents 29 cells and the green curve represents 15 cells 55

4.11 An equivalent circuit of light spot on a solar cell 57

4.12 A schematic diagram of light beam induced current (LBIC) experiment setup 58

4.13 Two dimensional view of open circuit voltage at each point of a solar cell surface which was diced partially and then cleaved through 60

4.14 Three dimensional view of open circuit voltage at each point of a solar cell surface which was diced partially and then cleaved through 61

4.15 Three dimensional view of I_{sc} short circuit current at each point of a solar cell surface which was diced partially and then cleaved through 63

4.16 Three dimensional view of P_{max} at each point of a solar cell surface which was diced partially and then cleaved through 64

4.17 Three dimensional view of V_{oc} for a solar cell which was diced through 65

4.18 Three dimensional view of I_{sc} for a solar cell which was diced through 66

4.19 Three dimensional view of P_{max} for a solar cell which was diced through 67

4.20 Schematic diagram of the traveling light spot diffusion length measurement 68

4.21	Schematic diagram of the traveling light spot diffusion length measurement	69
4.22	Logarithm of short-circuit current as a function of laser spot position. . .	70
4.23	Logarithm of short-circuit current as a function of laser spot position for solar cell cut through	72
4.24	Logarithm of short-circuit current as a function of laser spot position for solar cell patriotically cut and then cleaved through	72
4.25	A diagram shows maximum output power at different location of the solar cell die surface	75
4.26	Saturation current of reverse biased solar cell die diced fully through . .	77
4.27	Saturation current of reverse biased solar cell die diced partially and cleaved through	77
4.28	Shunt resistance at each operating point for cells which were partially diced and cleaved through	78
4.29	Shunt resistance at each operating point for fully diced cells	79
4.30	A schematic diagram of measurement of the determination of angle de- pendence of solar cell performance	80
4.31	Effective absorption area of a surface when incident angle is θ	81
4.32	A comparison of a theoretical curve and measured data	82
4.33	Parameters of a plano-convex lens	82
4.34	A comparison of P_{max} measurements with a lens and without a lens . . .	83
4.35	A simulation using OpticsLab software	85
4.36	Power output vs angle at different lens-cell space	85

6.1 Schematic diagram showing cross section view of the structure and components of a flexible silicon solar cell	90
---	----

List of Tables

1.1	Band gap energy and material for a triple junction cell	11
4.1	Plano-Convex Lens	83
4.2	Integration comparison	84

Chapter 1

Introduction

1.1 Development of silicon solar cell

In 1839, Edmond Becquerel first discovered that shining light onto a silver coated platinum electrode in an electrolyte could produce electric current[1,2]. This is considered to be the first observation of the photovoltaic effect. In 1894, Charles Fritts fabricated the first working solar cell by forming a very thin gold layer on a semiconductor material selenium[3]. An asymmetric electric junction is formed between the semiconductor and the metal to separate electron-hole pairs. All these photovoltaic devices rely on behavior due to the Schottky barrier existing between the semiconductor and metal layers. The discovery of photovoltaic properties of different materials triggered scientists' interests for energy conversion of sunlight to electricity. The idea of using a solar cell as an alternative energy source was not implemented until the 1950s when the development of silicon based electronics led to the requirement of highly purified silicon material. It was realized that the simple p-n junction structure in silicon is able to demonstrate a rectifying effect which exhibits excellent photovoltaic (PV) behaviour as a photocell. In 1954, D. M. Chapin, C. S. Fuller, and G. L. Pearson from Bell laboratory reported the first silicon p-n junction solar cell of an approximately 6 % efficiency[4].

The conversion efficiency of this newly invented solar cell was considerably higher than the early solar cells. The early development of the silicon solar cell was also

leveraged by the space application because the solar cell was the only long term power source that could facilitate power generation in the remote areas such as a satellite in space[5]. In the 1970s, the global oil crisis further warned the world of the urgency of developing alternative energy sources[6]. Industry started to show interest in new energy sources and support terrestrial solar cell research and development. Over the past two decades, the solar cell industry has experienced annual growth rates of about 15 to 20 %[3] and the production cost of solar cells has decreased significantly. The falling price of solar cells is making them an attractive means to generate electricity in remote areas when provision of conventional electrical power is too expensive. Solar energy, a renewable and clean energy source, introduces less green house effect, global warming risks and pollution than do conventional fossil fuels. In the 1980s, the first silicon p-n solar cell of efficiency over 20% was reported by Martin Green et al. at the University of New South Wales (UNSW) [7]. Currently, the highest crystalline silicon based solar cell is the PERL cell with a conversion efficiency of 24.7% [8]. Large modules with efficiencies above 20% are available in the market[9].

Silicon has long been recognized as the primary solar cell material. Nowadays, more than 90% of the solar cell market uses silicon based cells. Single crystalline and polycrystalline silicon solar cells compose the main portion of the solar cell market[10].

Two silicon material manufacturing methods are widely used in the PV industry[11]. One is the Czochralski method which is more cost effective but produces less purified silicon and therefore is preferred by the PV industry for manufacturing commercial solar cells[12]. The other silicon crystalline growth method is the float-zone method. The float-zone method produces silicon material which is higher in purity but more costly[13]. P type dopant (boron) is doped during the growth. The grown single crystal ingot is sliced into wafers and etched to smooth the surface. There exist several ways to form p-n junctions. The already p-doped wafers are n type doped by

diffusing phosphorus at high temperature or through ion implantation which allows a greater control of the doping profile. A p-n junction is formed at under one micron depth below the surface. Front and rear metal electrodes are formed by the screen printing method at high temperature[14]. Polycrystalline silicon is also another important solar cell manufacturing material which is usually formed grown by casting methods or by ribbon growth methods[15]. A front n doped surface requires surface texturing to reduce the reflection of the incident light by forming an antireflection coating. The back surface of the solar cell is heavily doped to create a back surface field which helps to reduce carrier loss through surface recombination. The low cost screen printing approach enables an easy way to make front contacts[14]. Technology of this type of solar cell has already been well established.

Single crystal and multi-crystalline silicon are the best-known solar cell materials due to their excellent stability and proven performance in the field, yielding 14-20% conversion efficiency in production[16,7], and up to 25% in the laboratory[8]. Figure 1.1 illustrates the development of silicon solar cell in terms of laboratory efficiency record.

Solar cell technology was highly developed for space application in the 1950s. In order to maximize radiation resistance, 10 ohm-cm p type substrate was used. Another feature is a 40 ohm/square, 0.5um deep phosphorus diffusion[17]. An efficiency of 10 to 11% was achieved through this structure which became the standard cell for space application. In the 1960s, a rear Al treatment boosted the efficiency up to 12.4%. The increase of efficiency is due to the reduction of effective rear surface recombination. In the early 1970s, a series of design changes of the solar cell structure greatly improved cell efficiency 30% in performance compared to the conventional cell and these changes directly led to a "violet cell"[18]. Better antireflection coatings were used to improve current output and gave the cell a violet appearance. A

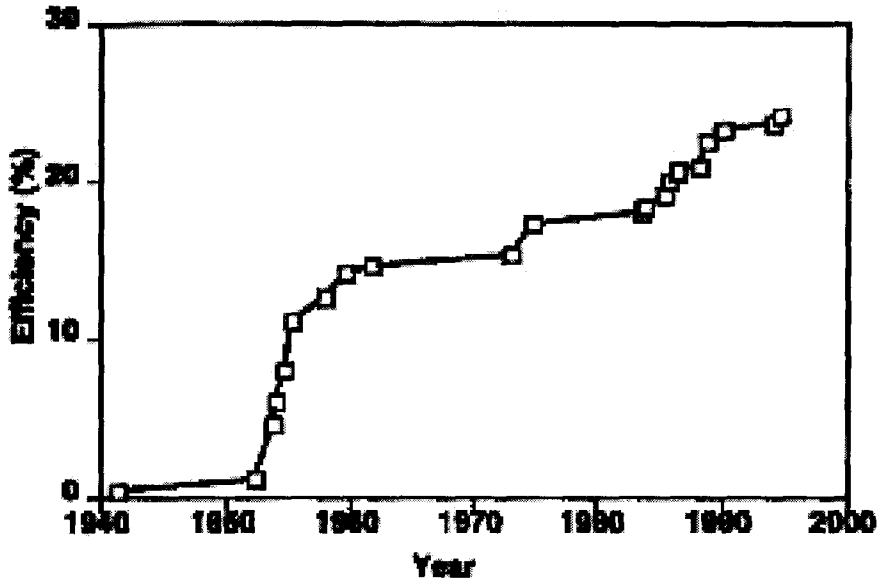


Figure 1.1: Evolution of silicon laboratory cell efficiency.
[14]

shallow junction (25 μ m) was incorporated into the cell design to remove "dead layers". Finer front metal finger patterns were introduced by using photolithography to lower cell resistance. Lower substrate resistivity gave an increase of open circuit voltage. Shallow junctions, improved anti-reflecting coatings, and lower top contact area led to a higher output current. A sharper IV characteristic curve attributed to improved open circuit voltage and decreased cell series resistance resulted in a higher energy conversion efficiency. Under radiation in space, the conversion efficiency was increased to 13.5% and terrestrial efficiency achieved 16%[7,14].

Four types of silicon terrestrial solar cells are introduced to demonstrate the development of silicon solar cell technology:

Black Cells

The black cell was developed in the early 1980s with a conversion efficiency of 17%. One noticeable feature of this cell is the texture of the front surface[19].

The surface of the black cell is anisotropically etched to expose (111) crystallographic planes on a (100) silicon substrate to form square based pyramids. These pyramids are distributed randomly on the surface of the solar cell to greatly reduce the reflection. The pyramids increase the chance of the incident light being reflected towards the cell. Light will have a long optical path length thus improving optical absorption by coupling more light into the cell[3,7,20].

PESC

The PESC stands for passivated emitter solar cell which was designed at University of New South Wales (UNSW) with a efficiency over 20%[7]. A cross section view of PESC is shown in figure.1.2

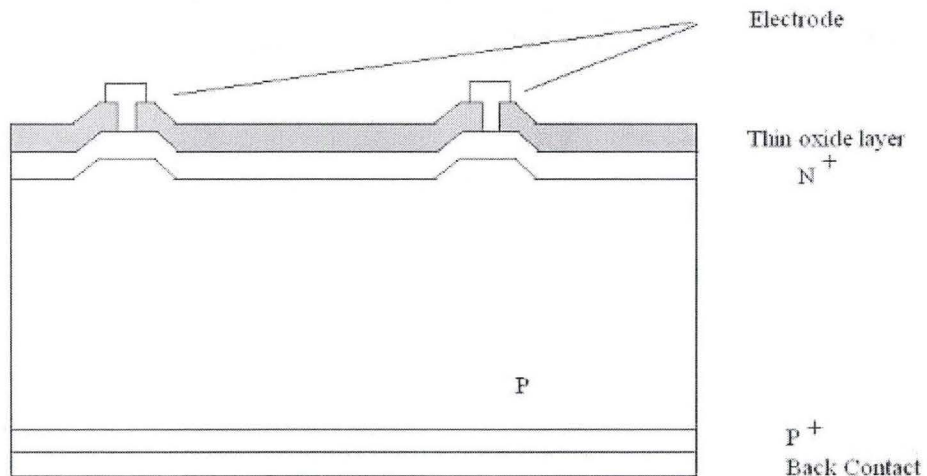


Figure 1.2: A cross section view of PESC [3]

The front electrode is in contact with the heavily doped n region through a slot in the thin oxide layer. The top shallow junction is formed by diffusing phosphorus into the p type silicon layer which is grown by the float-zone method. A thin silicon dioxide layer is grown to passivate the front silicon surface. Photoresist is used to define the front contact area to minimize the surface recombination at the metal-semiconductor interface. Microgrooves are formed on the top surface instead of pyramidal texturing

for antireflection of the incident light. The performance of the PESC cells is higher than that of black cell due to the improved top surface and contact passivation by growing the oxide layer and minimizing electrode areas[3,7].

Back contact cells

The Back contact cell shown in fig.1.3 was introduced at Stanford University and originally designed for concentrator solar cell purposes. An efficiency of 22.2 % was reported at one sun condition. Since both n contacts and p contacts are formed at the back of the cell, there are no electrodes at the front surface to block incident light. The n and p regions at the back side are heavily doped to form point contacts as shown in fig.1.3. The back surface is passivated to form an oxide layer which can reduce the back surface recombination. The heavily doped n and p points create an electric field to separate the electron-hole pairs. This structure greatly reduces the large recombination between the semiconductor and metal interface by reducing their contact area. The front surface is also passivated with an oxide layer to minimize the front surface recombination. The front surface is textured to reduce the reflection of incident light. Front and back surface are doped by diffusion to create a built-in field so that generated carrier pairs can be repelled from the surface; therefore, surface recombination can be reduced in this way [3,7,20,21].

The incident light absorbed in the high quality n type silicon material grown by the float-zone method generates electron-hole pairs. The electron-hole pairs diffuse to the back side and are separated by the small built-in electric field created from heavily doped n and p regions. Thus the quality of the n type silicon material plays crucial a role in the carrier collections. High diffusion lengths for the carriers is the key to ensure enough generated carriers survive and diffuse to the back junction field.

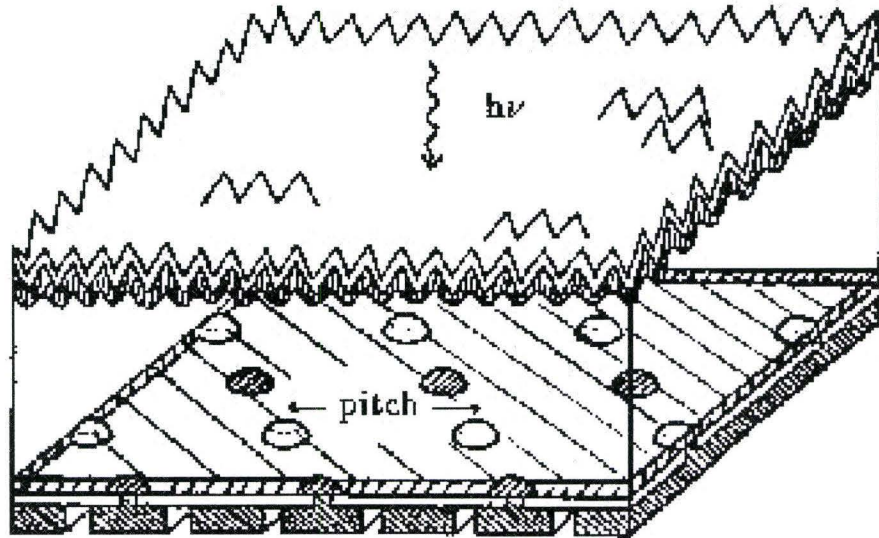


Figure 1.3: A schematic structure of back contact cell
[20]

PERL

The highest conversion efficiency record 24.7% has been held by the PERL cell reported from the University of New South Wales[8]. PERL stands for the passivated emitter, rear locally diffused solar cell. The main structure is shown in figure 1.4. The front surface is textured with an inverted pyramid structure to increase the chance of the incident light being reflected into the cell. An antireflection coating is deposited to further reduce the surface reflection. The front surface defect states can be reduced by growing an oxide onto the n type emitter material to passivate the surface so as to reduce the front surface recombination. Near the front contact, the n type material is heavily doped to form an ohmic contact. The back surface is passivated with an oxide layer and the back point contacts are locally diffused to reduce the metal-semiconductor interface which leads to a high recombination rate. The silicon substrate is grown using the float-zone method. [3,14,22].

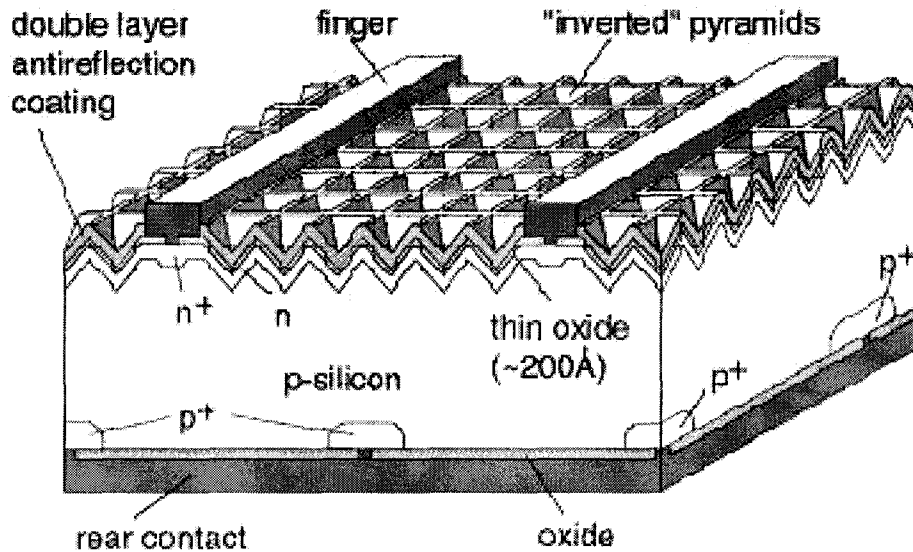


Figure 1.4: PERC structure
[22]

1.2 Flexible solar cell

Two types of existing solar cells can be considered flexible solar cells. One is the thin film inorganic solar cell and the other type is organic solar cell. Among various types of thin film solar cells, the amorphous silicon (a-Si) solar cell is the one that has been most successfully scaled up to large area product from laboratory prototype and has been made commercially available. Organic solar cells are still under investigation in many laboratories on the world and the highest efficiency is not much greater than 6% [23]. Brief histories, structures, advantages and existing challenges of these two types of flexible solar cells will be discussed.

A very high efficiency to cost ratio makes the thin film solar cell desirable when they are compared with bulk crystalline silicon solar cells. One advantage of thin film solar cells is that their active regions are, at most, only a few microns thick, so source material cost can be kept very low. Another advantage is that many existing deposition techniques can directly match the thin film solar cell requirements. A variety of thin film growth methods have already been widely employed in photovoltaic

research and manufacturing and these methods play a very important role in the investigation and production of various types of thin film solar cells.

1.2.1 Amorphous silicon solar cell

The amorphous silicon (a-Si) solar cell has been improved in the past twenty years and it reached a power output of 35 megawatts in 2000 [24]. Carlson and Wronski invented the first a-silicon solar cell with a conversion efficiency of 2.4% [25]. However, prior to the invention of the first a-Si solar cell, many researchers had devoted themselves to the study of characteristics and growth of a-Si material. The deposited thin film is a hydrogenated amorphous silicon based alloy (a-Si:H) with high optical absorption (10^5cm^{-1}) and its band gap can be changed in a range from 1.1eV to 2.5eV which makes this type of material suitable for photovoltaic applications[24]. The a-Si:H conversion efficiency is strongly affected by the so called Staebler- Wronski Effect (SWE): a change of initial efficiency by 10-20% when the a-Si:H solar cell is exposed to the sunlight[26]. In order to reduce the SWE, a possible approach is to keep the active layer thin [14,24].

The operation of the a-Si solar cell is no different from a crystalline silicon solar cell. An intrinsic layer of undoped a-Si:H or a-SiGe:H materials (absorption region) is sandwiched between p-type doped Si:H and n-type doped Si:H [14] as shown in fig. 1.5.

When photons of sufficient energy pass through the intrinsic region, electron-hole pairs are generated and these charge carriers are transported to p side and n side respectively by the built-in electric field. Since the dopants will introduce defects states at midgap which limit the free carrier lifetime, the intrinsic region is not doped [14]. Investigations have shown that p-type a-SiC:H can form p-type layers which

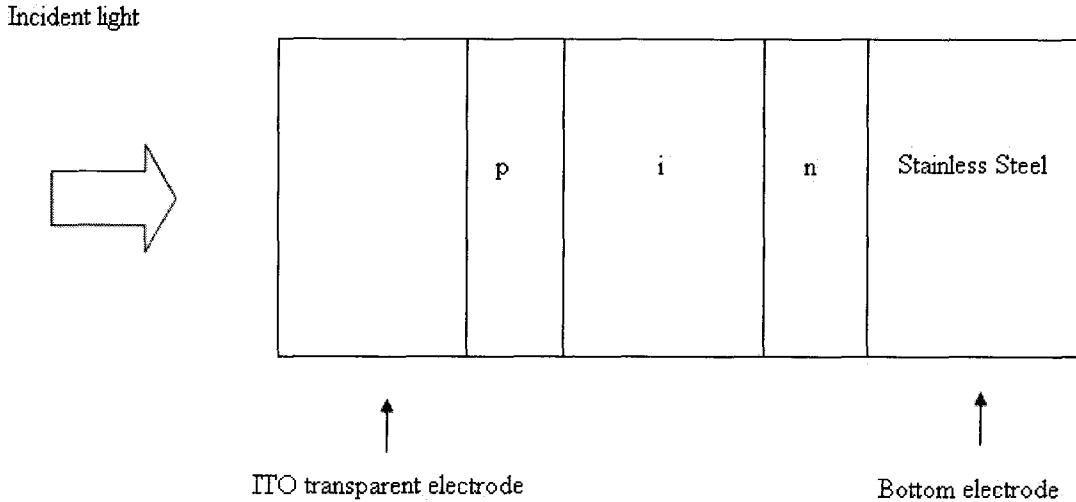


Figure 1.5: A schematic diagram of a-Si solar cell

have quasi-fermi levels about 0.4 meV to 50 meV from the valence band and the n-type a-Si:H and n-type microcrystalline-Si:H ($\mu\text{c-Si:H}$) form excellent n-type film layers which have their quasi-fermi level 0.2eV to 50meV from the conduction band; therefore a p-i-n structure can be built using these materials [14].

Early deposition of a-Si:H was mainly carried out by DC and RF PECVD using silane as the source material. However, due to the low growth rate (10-20 nm /s), deposition techniques with higher deposition rate were employed, such as very high frequency PECVD. A deposition rate of 100 to 150 nm/s can be achieved via this method [24]. Two even higher rate deposition techniques were developed: hot-wire CVD (HWCVD) and the atmospheric pressure plasma CVD.

Table 1.1: Band gap energy and material for a triple junction cell

Layers	Intrinsic lay bandgap	Intrinsic layer material
Top Cell	1.8 eV	Si:H
Mid Cell	1.6 eV	Si:Ge:H
Bottom Cell	1.4 eV	Si:Ge:H

There are four steps involved in the a-Si alloy deposition[14]:

1. Dissociation of the source gas silane and hydrogen molecules by electron impact
In this step the silane is dissociated into a mixture of ionized molecules, which are reactive
2. The transportation of dissociated source gas to the substrate via gas diffusion
3. The reaction of the molecules on the surface to grow film
4. Etching off and pumping off reaction byproduct

Most commercially available a-Si solar cells are single junction, double junction or triple junction cells [27]. A triple junction solar cell device has been designed and fabricated at United Solar System Corporation[27]. This type of cell has three different band gap absorption layers, which can split the spectrum accordingly from top to bottom: the three cells absorb blue, green and red lights respectively. Table 1.1 shows three i-layer materials and band gap [24].

United Solar has built up a roll-to-roll product line for manufacturing triple junction a-Si solar cells as shown in figure 1.7. There are nine chambers along the product line and each of them is responsible for depositing one specific layer material onto a stainless steel web. The structure and material for each layer is shown in figure.1.6 Each layer is deposited using PECVD at 1 Torr and all the deposition processes in nine chambers are carried out simultaneously and the stainless web moves through nine chambers to complete a full triple junction structure[27].

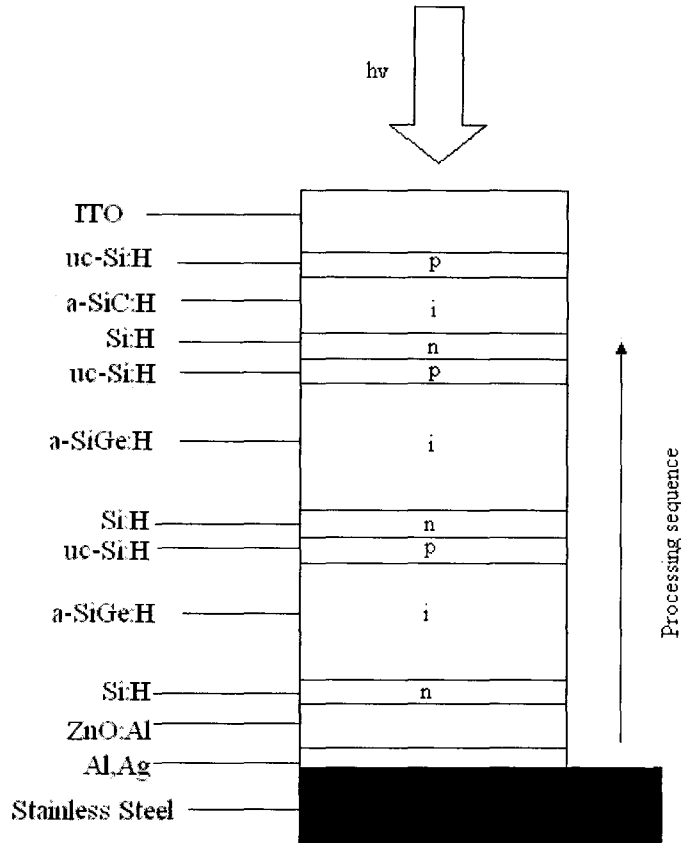


Figure 1.6: Structure for a triple junction a-Si solar cell. The material for each layer is labeled

[14,24]

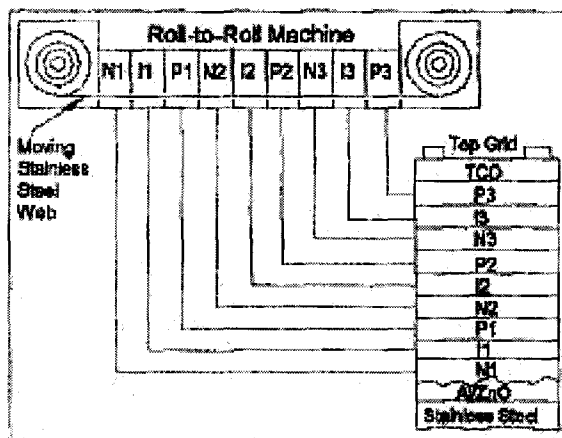


Figure 1.7: A roll-to-roll operation for the deposition of a triple junction solar cell

[27]

On a stainless steel substrate, the nine layers are listed below from bottommost n type layer of the bottom cell to topmost p layer of the top cell:

1. 20nm phosphors doped a-Si:H n layer
2. 130nm a graded a-SiGe:H i-layer
3. 10nm boron doped microcrystalline Si:H p layer
4. 10nm of phosphors doped a-Si:H n layer
5. 110nm a graded a-SiGe:H layer i-layer
6. 10nm boron doped microcrystalline Si:H p layer
7. 10nm phosphorus doped a-Si:H a:Si:H n layer
8. 100nm a-Si:H i-layer
9. 10nm boron doped microcrystalline Si:H [14].

Energy Conversion Device(ECD), which cooperated with United Solar with a 30 MW production in 2002, is also involved in large scale a-Si solar cell manufacturing and a production of about 30% per year increase is reported by ECD [28].

Since the first commercial a-Si solar cell was invented to power the pocket calculator 20 years ago, the amorphous silicon solar cell has been greatly improved by many research groups and also has become accepted by society as an alternative renewable energy device. However, in order to compete with other types of solar cells and energy sources, many remaining problems still have to be solved in the future. Remaining challenges include further improving stabilized conversion efficiency, lowering manufacturing costs, and extending a-Si solar cell's long term stability. The ability to answer and solve these issues relies on new approaches to design for the next generation of solar cells, including the novel multi-junction structure involving both a-Si and microcrystalline Si [14]. New deposition methods with higher deposition rates and lower material cost will also be of crucial importance.

1.2.2 Organic solar cell

Organic material for use in electronic purposes has been developed over the past three decades[29,30]. There has been increasing interest in organic materials used for solar cell purposes in the past few years. The newly discovered conjugated polymer blended structure increases the conversion efficiency to 6% [23]. The advantages of low printing cost, large area and high throughput manufactured via reel to reel deposition makes the organic solar cell very attractive[14]. Organic solar cells also have the advantage of flexibility.

There are many obvious differences between organic material and inorganic material for solar cell use. Photo-generated electron-hole pairs are strongly bonded by coulomb force in a form of excitons. Therefore, absorbed light does not contribute directly to the charge carrier separation. For organic semiconductor material does not have band structure similar to that of inorganic materials and the existing Van der Waals forces bonding the molecules together is very weak. Charge carrier transport in the organic material is completed through a hopping transport process between localized states. The electron and hole mobilities, therefore, are about 10^5 times lower than that of the inorganic material such GaAs and Si. Organic solar cell material is easily degraded under oxygen and water. The narrow absorption spectrum compared to the solar spectrum limits the output photocurrents[14]. The organic solar cell is still at its early developing stage and more research must still be devoted to this new field.

1.2.3 Flexible silicon solar cell in this thesis

This newly invented flexible solar cell demands less material for a similar conversion efficiency. The merit of flexibility can resolve the fragile problems of the

conventional solar cell and this property has great potential to lower assembly cost. The novel (partially dice and cleave through) PDCT method introduces much less defects to the solar cell material and can significantly reduce the cell efficiency loss due to the dicing process. These advantages have the potential to greatly reduce the material cost and mounting labor cost which make it a good candidate to replace conventional solar panels.

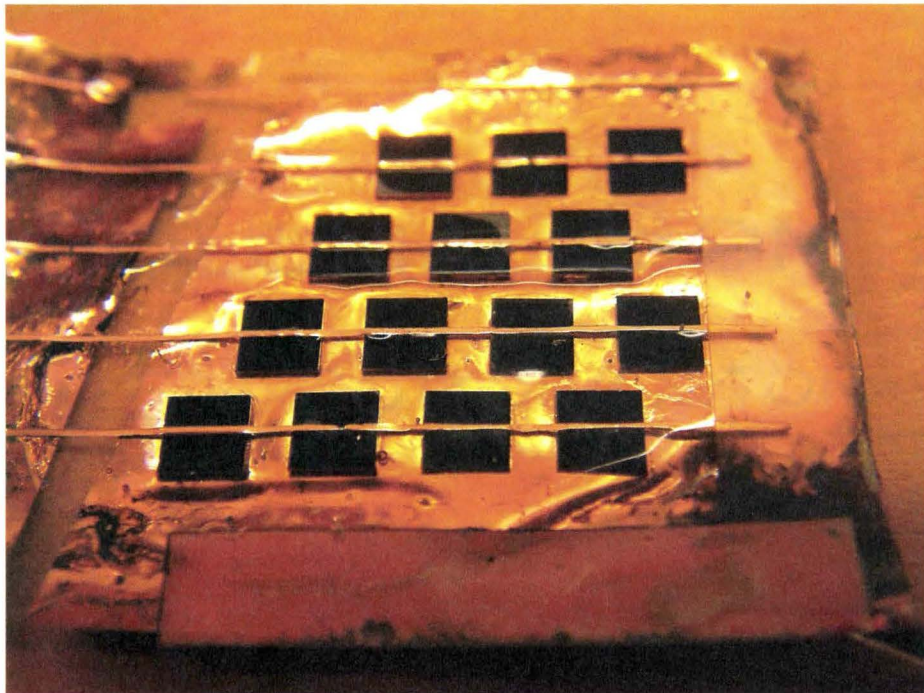


Figure 1.8: Flexible solar cell

As shown in figure 3.1, 2.5mm by 2.5mm solar cell are patterned in a designed array. The top electrodes of these die are interconnected through the copper wires which are grown on a TEFZEL film and epoxy fills the space between the dice. A copper layer is grown at the backside of the die and epoxy to form a back electrode. For the last step, a lens array is mounted on top of the TEFZEL above to focus the light on the solar cell die. The progress so far is that a solar array prototype has been successfully completed and further work will rely on the selection of a proper lens array and enlargement of the prototype size.

1.2.4 Comparison of three types of flexible solar cell

A comparison of three types of flexible solar cell, amorphous silicon solar cell, organic solar cell and flexible solar cell in this thesis is now presented.

The technology of manufacturing a-Si solar cells is mature in industry. United Solar has already been able to make roll-to-roll production of triple junction a-Si solar cells on a stainless steel substrate using PECVD film growth deposition techniques. A stabilized conversion efficiency for a single junction a-Si solar cell can achieve 6 to 8 % [14]. The future of a-Si solar cell depends on the ability to resolve several problems with a-Si solar cells.

First, the initial efficiency of a-Si is not stable. As mentioned before, the Staebler-Wronski Effect lowers the initial conversion efficiency by 12 to 20 % when the cell is exposed to sunshine. This light induced degradation of the solar cell has not been fully understood. Research and development are needed reduce the efficiency degradation [14,24].

Second, manufacturing equipment and facilities for a-Si thin film growth makes the capital cost of the a-Si solar cell relatively high. The cost could be lowered by increasing the throughput of equipment. However, the deposition rate of the thin film is low, and a higher deposition rate is required to improve the throughput.

Third, the long-term reliability of a-Si solar cell is questionable. Crystalline or poly crystalline silicon solar cells have more than 20 years of reliability. The most recent manufactured a-Si solar cells cannot endure such a long period reliably. More research and development are necessary to ensure a-Si solar cells survive over 20 years in hot and humid climates [14].

Fourth, the commercial a-Si solar cell efficiency of 6 to 8% is still much lower than 14 to 18 % of single crystalline or poly-crystalline silicon based commercial solar cells. Considerable effort should be put to improving the conversion efficiency.

The organic solar cell is still at its early development stage with emphasis still on searching for new organic materials for photovoltaic purposes. The highest laboratory scale cell efficiency is around 6 % [23]. There is no commercially available organic solar cell on the market. However, its advantage of being able to use roll to roll printing manufacturing technique may make its capital cost very low. Many issues related to organic solar cells need to be resolved. Organic solar cells suffer from severe degradation under sunshine and oxygen. The mobility of charge carriers is also very temperature dependent. All these increase the instability of electrical performance of organic solar cells. In order to prevent the organic solar cell from degradation due to moisture and oxygen, a hermetic encapsulation is required to seal the cell. Considerable improvements are still needed to ensure long term stability and higher conversion efficiency for organic solar cells for commercial use.

The flexible solar cell in this thesis is based on existing crystalline silicon solar cell technology. Commercial solar cells are diced into appropriate small solar cell die which are mechanically and electrically bonded onto a transparent flexible substrate with corresponding electrodes. The space between mounted die is filled by epoxy which allows certain degrees of flexibility when the sample is bent. Since the active solar cell die in the sample are directly diced from the proven commercial solar cells, the reliability and conversion efficiency are ensured. There is less problem with light induced degradation in this new solar cell since the flexible substrate Tefzel is an already-proven UV tolerant material. The new structure offers this flexible solar cell sample flexibility while maintaining good conversion efficiency. There are, however, some issues related to this new flexible solar cell structure. First, there is inevitable

efficiency loss during the dicing process. However, in the chapter of Experiment and Discussion , dicing methods which reduce the efficiency loss will be discussed . Second, the spaces between the solar cell die do not contribute to the total output current and voltage. In the Future Work section, an extra lens structure which refracts light onto the active solar cell die area from the epoxy area will be discussed. Therefore, this new structure will offer a better flexible solar cell with a high reliability, high efficiency and a long term stability compared with the a-Si solar cell and organic solar cell.

Chapter 2

Theory

2.1 Basic concepts of solar cell

A solar cell is a device which generates electricity by converting sunlight energy into electrical energy with high conversion efficiency. The highest conversion efficiency for silicon- based solar cells is around 24 percent [8]. Most commercial silicon solar cells have efficiencies ranging from 14 percent to 20 percent[7,16]. Since solar power can be considered unlimited for human use, solar cell provides an excellent means to utilize this solar energy source. Typically, a conventional solar cell is a p-n junction device with a large surface area which can sufficiently capture solar radiation and thus generate electron-hole pairs. The excess electron-hole pairs diffuse into the junction region and then are separated by an internal built-in electric field, thus contributing to the output current. A schematic structure of a solar cell is shown in fig. 2.1.

In a dark environment, a solar cell exhibits a diode-like electrical characteristics. Under an external bias, a solar cell allows large current to pass through for forward bias and limits the current to pass through for a reverse bias. If there is no external bias applying to the solar cell, it stays at an equilibrium condition and there is no output from the solar cell. In an illuminating condition, this equilibrium does not exist any more. The excess photo-generated electron and hole pairs split the original Fermi level into two quasi-Fermi levels at n and p regions. The built-in voltage V_o is lowered accordingly. Generated electron-hole pairs within the quasi-neutral regions

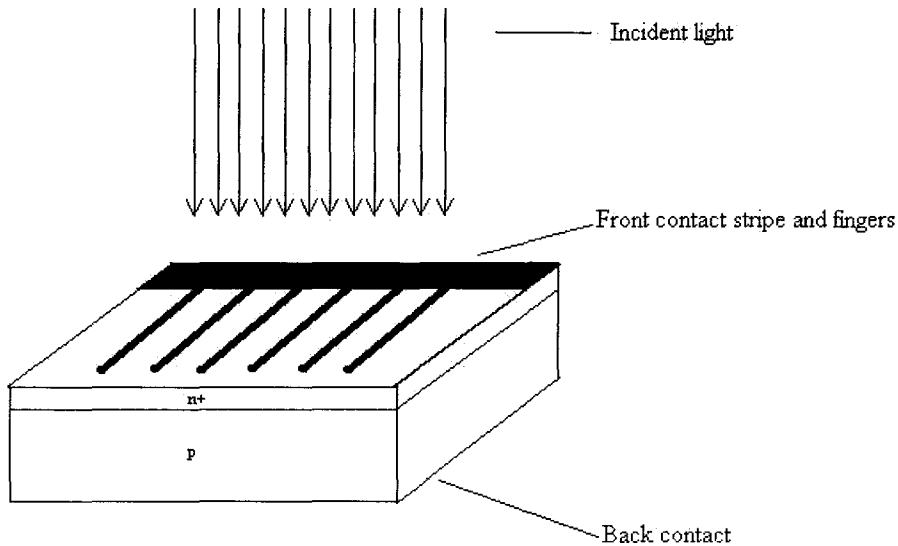


Figure 2.1: A schematic diagram of a typical solar cell structure

diffuse into the depletion region and then are swept across the built-in electric field to contribute to the photo-generated current. Since the built-in voltage is lowered, more thermal generated carriers at both p and n side can overcome potential barriers at the junction; therefore, the amount of dark recombination current, which is in an opposite direction with photo-generated current, is also increased. When a steady state is reached, the voltage that appears at two terminals of the solar cell become the same value as the potential difference between two quasi-Fermi levels. This output voltage generated at two terminals of a solar cell under illumination is known as the photovoltaic effect. The voltage appearing the two terminals with no load is defined as open circuit voltage V_{oc} . The current generated from a solar cell when its two terminals are directly connected is defined as short circuit current I_{sc} . A typical I-V characteristic of a solar cell in the light is illustrated in fig.2.2, in which the blue curve represents the output current at a different output voltage and the pink curve represents the amount of output power from the solar cell at different operating points. Notice the highest point of the pinkish curve indicates the maximum output power.

The corresponding I-V characteristics of an ideal solar cell is a linear combination of photo-generated short circuit current and dark recombination current. The solar cell IV equation is then commonly formulated as[3]:

$$I = I_{sc} - I_o(\exp(qV/k_B T) - 1) \tag{2.1}$$

Where

I represents the output current to an external circuitry,

I_o represents the thermally generated current

I_{sc} represents the short circuit current

V represents the output voltage to the external circuitry

k_B represents the Boltzmann's constant

T represents the operating temperature of the device

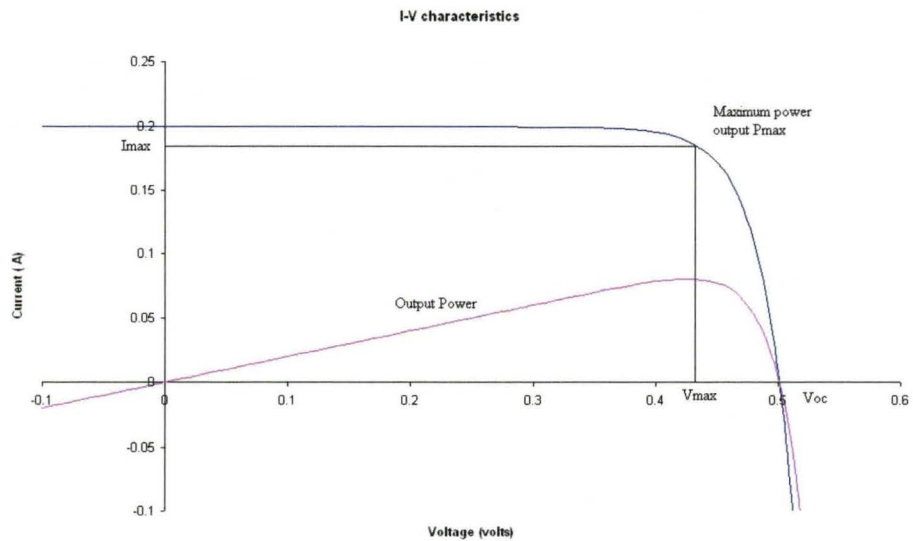


Figure 2.2: I-V characteristics and the output power of a solar cell

The behaviour of a solar cell under illumination can be modeled as a current source which is in parallel with a normal diode. An equivalent circuit for an ideal solar cell (neglect all parasitic resistance) is illustrated in fig.2.3

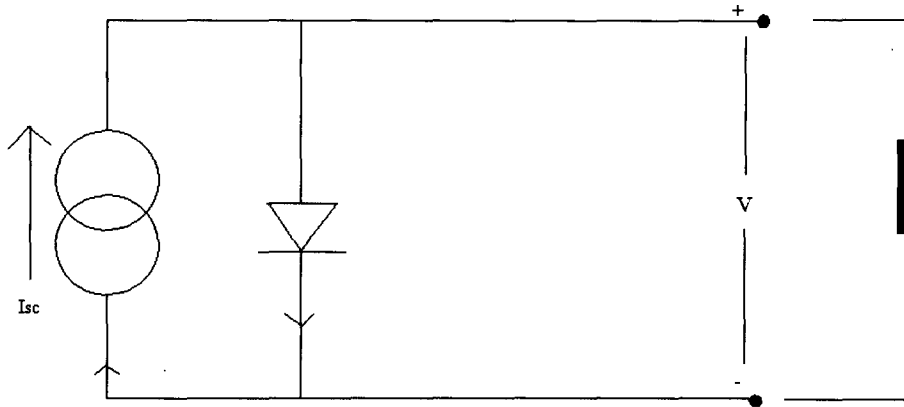


Figure 2.3: Equivalent circuit of an ideal solar cell
[31]

Output voltage is provided from the diode in fig.2.3 and adjusting the load resistance can affect the amount of current flowing through the diode thus changing the output I-V characteristics. The amount of output current to the external circuitry depends on the load resistance R_L by equation: $I = V/R_L$. In a dark condition, I_{sc} is equal to zero and no electron-hole pairs are optically generated, thus no current passes through the diode; the output voltage then is also equal to zero. When the solar cell is under a constant illumination, the short circuit current is divided between the diode and the external circuitry[32].

According to equation 2.1, when the load resistance is equal to zero, then output voltage V is equal to zero and output current I has become short circuit current I_{sc} . Since the solar cell is short circuited, the output current must be I_{sc} . When the load resistance R_L is infinitely large, the output current becomes zero[32].

When the solar cell is open circuit, the output current is zero and an open circuit voltage V_{oc} is generated as shown in equation 2.2.

$$V = V_{oc} = \frac{k_B T}{q} \ln\left(\frac{I_{sc}}{I_o} + 1\right) [33] \quad (2.2)$$

By properly choosing load resistance, a maximum power output can be extracted out from the solar cell as illustrated in fig.2.2. If V_{max} and I_{max} are defined as the corresponding output voltage and current for the maximum power point, the maximum power output is the product of them:

$$P_{max} = V_{max}I_{max} \quad (2.3)$$

This is the operating point for a solar cell to provide the largest amount of power to the external circuitry by selecting the optimum load resistance. The ratio of the P_{max} and the product of the I_{sc} and V_{oc} , and then the fill factor can be defined as

$$F.F. = V_{max}I_{max}/(I_{sc}V_{oc}) \quad (2.4)$$

Silicon solar cells commonly have F.F. around 80 percent [31]. The conversion efficiency is defined as:

$$\eta = V_{max}I_{max}/AP_{in} \quad (2.5)$$

where P_{in} is the incident solar power density onto the solar cell with a surface area of A. The equation then can be rewritten as in a more compact form:

$$\eta = V_{max}J_{max}/P_{in} \quad (2.6)$$

where J_{max} is the current density at the maximum output power point.

2.2 Diffusion length calculation from light beam induced current scanning

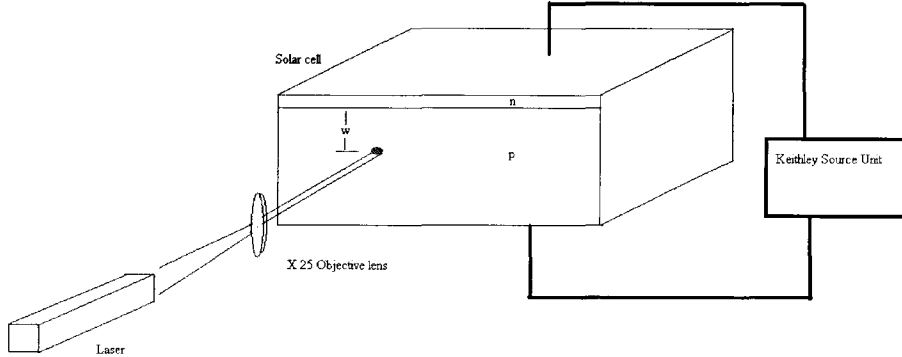


Figure 2.4: A schematic diagram of a focused light beam on the edge of a solar cell

The diffusion length L_n of minority electrons in the n region of a p-n junction silicon solar cell may be extracted by performing light beam induced current (LBIC) scanning[34,35]. When a focused monochromatic light beam with photon energy greater than the band gap of silicon is applied onto the edge of the solar cell as shown in fig.2.4, the short circuit current varies as a function of the light spot position on the edge of the cell. The photons that fall onto the edge of the cell will be absorbed. Assume the incident light intensity is ϕ_o in a unit of *photons/sec* – cm^2 which contributes to electron-hole pairs generation. In the p side of the cell, the minority carrier electrons at a distance w away from the junction will have a fraction proportional to $\exp(-w/L_n)$ diffuse to the junction. The number of light generated excess minority carrier electrons in the P side reaching the junction can be formulated by:

$$N \propto \phi_o \exp(-w/L_n) \quad (2.7)$$

The short circuit current in steady state is proportional to N . Then I_{sc} can be formulated by a product between a proportionality constant C and the right hand side of equation 2.7.

$$I_{sc} = C\phi_o \exp(-w/L_n) \quad (2.8)$$

Taking natural logarithm on both sides of equation 2.8 to obtain

$$\ln(I_{sc}) = \ln(C\phi_o) - w/L_n \quad (2.9)$$

Taking the derivative with respect to w , since the term $C\phi_o$ does not change with w , we obtain:

$$\frac{d \ln I_{sc}}{dw} = -\frac{1}{L_n} \quad (2.10)$$

The diffusion length of electrons in the P region is then given by:

$$L_n = -\left(\frac{d \ln I_{sc}}{dw}\right)^{-1} [34, 35, 36] \quad (2.11)$$

Theoretically there exists a linear region in the diagram of $\ln I_{sc}$ vs. w (the distance between the junction and the light spot). Therefore, if the I_{sc} is measured as a function of the position of the light spot, the diffusion length can be calculated from the slope of this linear region according to equation 2.11.

2.3 Short circuit current

A one-dimensional geometry experiment is set up as shown in fig. 2.7. The junction depth is d .

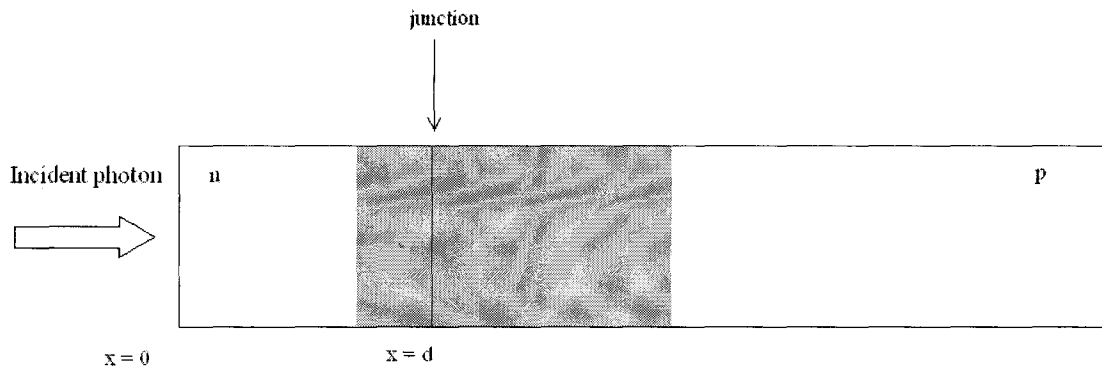


Figure 2.5: A schematic diagram of a one dimensional cross-section solar cell structure. d is the junction depth.

If the solar cell is illuminated by a light source of an intensity of ϕ_o at wavelength λ over the entire front surface, the short circuit current is then the integration of all the excess minority carriers across the cell reaching the junction. The light intensity transmitted into the cell at location x is given by $\phi(x) = T\phi_o \exp(-\alpha x)$ where T is the transmission coefficient at the front surface of the cell, ϕ_o is the incident photon density, and α is the absorption coefficient which is dependent on the wavelength and the material. The electron-hole generation rate at position x in the cell is just the absolute value of the derivative of $\phi(x)$ with respect to x . We get:

$$G(x) = T\alpha\phi_o \exp(-\alpha x) \quad (2.12)$$

In this case, the experiment can be treated as the integration of light beam induced current at all the positions across the p-n junction cell when comparing with light beam induced current (LBIC) scanning experiment.

The number of electrons reaching the junction and contributing to the short circuit current due to the photo-generated electron-hole pairs at position x in the n region is

the product of the photo generation rate at position x and an exponential term which accounts for the fraction of the generated carriers reaching the junction by diffusion. The total number of excess holes per unit time in the n region that contributes to the photo-generated current then is the integral of the number of the electrons over the whole n region[31]:

$$N_p = \int_0^d T\alpha\phi_o \exp(-\alpha x) \exp\left(-\frac{|d-x|}{L_p}\right) dx = \frac{\alpha\phi_o L_p}{\alpha L_p - 1} [\exp(-d/L_p) - \exp(-\alpha d)] \quad (2.13)$$

The total number of the excess electrons in the p region that contributes to the short circuit current per unit time can be obtained by taking the integral from $x = d$ to $x = \infty$ and change diffusion length L_p to L_n in equation 2.13 if we assume p region is thick enough. We get:

$$N_n = \frac{T\alpha L_n \phi_o \exp(-\alpha d)}{\alpha L_n - 1} \quad (2.14)$$

The total number of carriers contributing to the short circuit current is the sum of the N_p and N_n . For a light source of wavelength λ illuminating onto a solar cell, in the steady state, the short circuit current is directly proportional to the total number of carriers reaching the junction from both n region and p region by diffusion. Then the short circuit current density is equal to q (elementary charge) times N_{total} ($N_n + N_p$) per unit time.

$$J_{sc} = \frac{qT\alpha\phi_o L_p}{\alpha L_p - 1} [\exp(-d/L_p) - \exp(-\alpha d)] + \frac{qT\alpha L_n \phi_o \exp(-\alpha d)}{\alpha L_n - 1} \quad (2.15)$$

2.4 Semiconductor transport equations

The current density equations for electron and holes respectively are given by[3,33,37,38,39]:

$$J_n = q\mu_n nE + qD_n \frac{dn}{dx} \quad (2.16)$$

$$J_p = q\mu_p pE - qD_p \frac{dp}{dx} \quad (2.17)$$

The first terms on the right sides of the equations account for the presence of drift current and the second terms account for the diffusion current which is caused by concentration gradients in the material.

In the quasi-neutral p and n regions, the current is dominated by diffusion current and the drift component is negligible since the electric field in these region can be neglected. Electron and hole diffusion current equations can be respectively rewritten as:

$$J_n = -qD_n \frac{dn}{dx} \quad (2.18)$$

$$J_p = qD_p \frac{dp}{dx} \quad (2.19)$$

In one dimension, for a volume of $\Delta x A$ in the p or n region of a solar cell, from the conservation rule of charge carriers in the cell, we can get:

$$\frac{\partial n}{\partial t} = \frac{1}{q} \frac{\partial J_n}{\partial x} - U_n + G \quad (2.20)$$

$$\frac{\partial p}{\partial t} = -\frac{1}{q} \frac{\partial J_p}{\partial x} - U_p + G \quad (2.21)$$

The terms on the left side of the equations are the buildup rate of electrons or holes. The first terms on the right of the equation accounts for the increase of electron

or hole concentration in ∂x A per unit time. G is the volume rate of band to band generation of electrons and holes. U is the volume rate of band to band recombination of electrons and holes. The physics of these two continuity equations can be better understood through fig.2.6

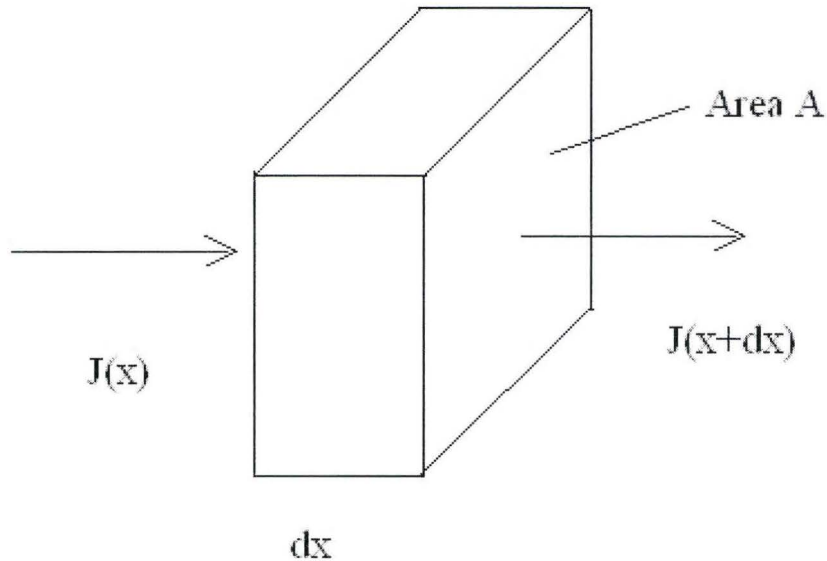


Figure 2.6: The amount of charge buildup in the differential volume $\partial x A$ is determined in three parts: the current passing through the volume, the E-H pairs generation rate in the volume and the E-H pairs recombination rate in the volume.

When a solar cell is in a steady state, the concentrations of electrons and holes do not vary with time, then we have:

$$\frac{\partial n}{\partial t} = \frac{\partial p}{\partial t} = 0 \tag{2.22}$$

Therefore in a steady illumination and electrical condition for a solar cell, the current density equations 2.20 and 2.21 can be written as

$$-\frac{1}{q} \frac{\partial J_n}{\partial x} = G - U_n \tag{2.23}$$

$$\frac{1}{q} \frac{\partial J_p}{\partial x} = G - U_p \tag{2.24}$$

The volume recombination rate for p-n junction solar cells can be approximated as [33]

$$U_p = \frac{p - p_o}{\tau_p} \quad (2.25)$$

$$U_n = \frac{n - n_o}{\tau_n} \quad (2.26)$$

Substituting equation 2.18 and 2.19 into 2.23 and 2.24 respectively, the current density equations become:

$$\frac{d^2 n}{dx^2} + \frac{n - n_o}{D_n \tau_n} + \frac{G}{D_n} = 0 \quad (2.27)$$

$$\frac{d^2 p}{dx^2} - \frac{p - p_o}{D_p \tau_p} + \frac{G}{D_p} = 0 \quad (2.28)$$

By properly choosing boundary conditions, electron and hole concentrations can be calculated from equations 2.27 and 2.28.

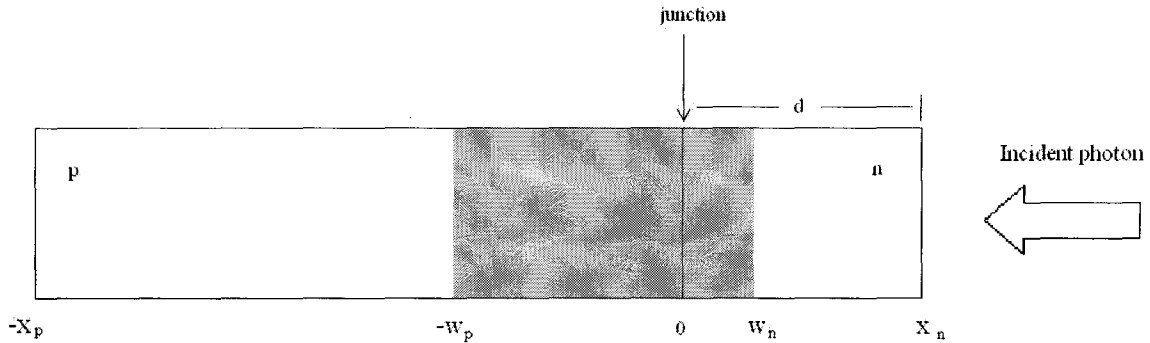


Figure 2.7: A schematic diagram of a one dimensional cross-section solar cell structure. $-w_p$ and w_n are the edges of depletion region. d is the junction depth. $-x_p$ and x_n are the edge surfaces of the p-n junction solar cell

In a dark condition, there are no optically generated electron-hole pairs and $G = 0$. Assuming thick n and p region, the excess electrons $n(x) - n_o$ and holes $p(x) - p_o$ at n and p regions can be expressed as [33]

$$n(x) - n_o = n_o (e^{qV/kT} - 1) e^{x/L_n} \quad (2.29)$$

$$p(x) - p_o = p_o(e^{qV/kT} - 1)e^{x/L_p} \quad (2.30)$$

When $G = 0$ and the solar cell is under a bias V , assuming n and p regions of the cell are long compared to the electron and hole minority carrier diffusion lengths, substitute equation 2.29 and 2.30 into equation 2.18 and 2.19 respectively. J_n and J_p can be approximated as

$$J_p(x = w_n) = \frac{qD_p}{L_p} p_o (e^{qV/k_B T} - 1) \quad (2.31)$$

$$J_n(x = -w_p) = -\frac{qD_n}{L_n} n_o (e^{qV/k_B T} - 1) \quad (2.32)$$

The total diffusion current density flowing through the solar cell under a bias V in a dark condition can be expressed as:

$$J_{diffusion} = J_p(x = w_n) - J_n(x = -w_p) = \left(\frac{qD_p}{L_p} p_o + \frac{qD_n}{L_n} n_o \right) (e^{qV/k_B T} - 1) \quad (2.33)$$

$$J_o = \left(\frac{qD_p}{L_p} p_o + \frac{qD_n}{L_n} n_o \right) \quad (2.34)$$

This is commonly referred to diode equation. when J_{dark} is multiplied by area A , then we get [3,33,40]:

$$I_{dark} = I_o (e^{qV/k_B T} - 1) \quad (2.35)$$

$$I_o = qA \left(\frac{D_p}{L_p} p_o + \frac{D_n}{L_n} n_o \right) \quad (2.36)$$

When the solar cell is illuminated by a light source of a wavelength λ , $i_{sc}(\lambda)$ may be approximated using equation 2.15

$$i_{sc}(\lambda) = \frac{qAT\alpha\phi_0 L_p}{\alpha L_p - 1} [\exp(-d/L_p) - \exp(-\alpha d)] + \frac{qAT\alpha L_n \phi_o \exp(-\alpha d)}{\alpha L_n - 1} \quad (2.37)$$

The short circuit current over the entire spectrum can be obtained by:

$$I_{sc} = \int_0^{\infty} i_{sc}(\lambda) d\lambda \quad (2.38)$$

The general form of solar cell equation thus is written as 2.1

$$I = I_{sc} - I_o(\exp(qV/k_B T) - 1)$$

2.5 Storage delay time

When the solar cell is forward biased in a steady state in a dark condition, there are excess minority carriers accumulated in the base region. When the forward bias on the cell is removed, these excess minority carriers cannot disappear immediately and the time for these charges to recombine in the cell is determined by storage decay time. This storage decay time is related to the lifetime of charge carriers and therefore, by measuring the storage decay time, the information of charge carrier lifetime can also be obtained through an equation which is derived in the theory part of this section[33].

In the circuit, a wave function generator is connected to a solar cell which is also in series with a 100 ohm resistor. The voltage from the generator at point A and the voltage across the resistor at point B as shown in fig. 2.8 are measured and compared.

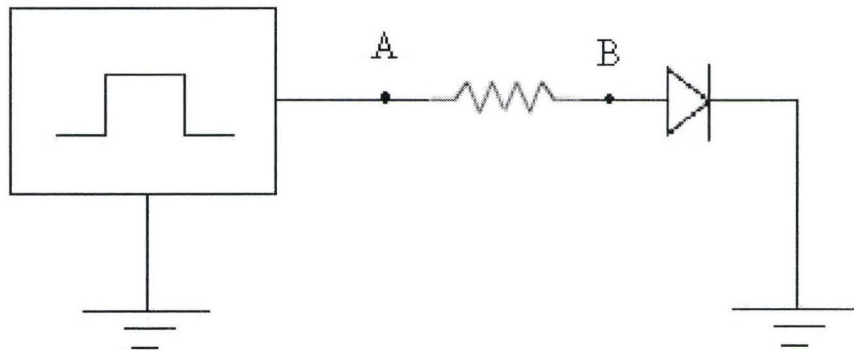


Figure 2.8: A schematic diagram of experiment setup for storage delay time measurement. The diode symbol represents a solar cell in a dark condition

Since the n region of a typical silicon solar cell is very thin and is much less than one diffusion length of the hole, the transient current here is considered to be due to the accumulated electrons in the p region.

For a diode subject to current i for $t < 0$ and $i = 0$ for $t > 0$, the storage charge distribution can be approximated by quasi-steady state. This approximation assumes that the decay of the storage charge remains a spatially exponential form.

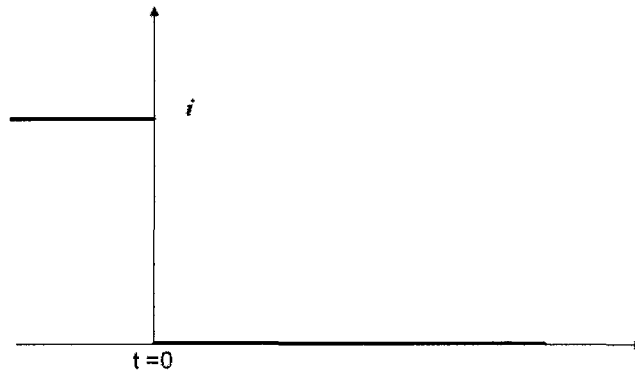


Figure 2.9: Current through the solar cell

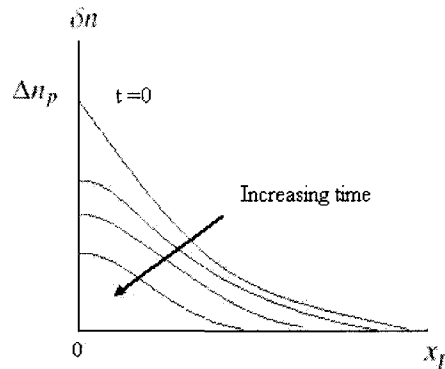


Figure 2.10: Excess electron distribution in the p-region as a function of time during the transient

[33]

In reality the current through the diode turns to zero when $t > 0$, which requires the slope of the excess carrier distribution at $x_n = 0$ being zero and thus this would distort the spatial exponential decay form of the storage charge as shown in the fig.2.10. The diffusion of excess charges will also change the exponential shape. In quasi-steady state approximation, these two conditions are ignored. δn remains an

exponential distribution at every instant time of the decay. Therefore, the total storage charge $Q_n(t)$ at time t in the p region may be expressed as:

Equations for $Q_n(t)$, the excess electron concentration is

$$\delta n(x_p, t) = \Delta n_p(t) e^{-x_p/L_n} \quad (2.39)$$

$$Q_n(t) = qA \int_0^\infty \Delta n_p e^{-x_p/L_n} dx_p = qAL_n \Delta n_p(t) \quad (2.40)$$

The instantaneous electron current can be expressed as:

$$i(t) = \frac{Q_n(t)}{\tau_n} + \frac{dQ_n(t)}{dt} [33] \quad (2.41)$$

where

$Q_n(t)$ represents the stored charge in the base region at time t .

τ_n represents the lifetime of the electrons in the p region.

$i(t)$ represents the transient current at time t .

The first term in 2.41 accounts for the recombination of excess electron and holes in the n type region and the excess carriers are replaced in τ_n . The second term in 2.41 accounts for the change of the excess carrier distribution with time. In the steady state, $dQ_n(t)/dt$ is zero[33].

In this experiment, an AC square wave signal is applied to a solar cell (2.5 mm by 2.5 mm) in the dark condition. The solar cell is connected in the circuit as shown in fig.2.8. The storage charge transient behaviour of the solar cell is observed when the applied voltage is switched from the forward bias to the reverse bias.

When the generator switches its output polarity from a forward bias V to a reverse bias $-V$, the current in the circuit turns to $I = I_r = -V/R$ initially and then becomes a very small current value. The large reverse current is unexpected since under the

reverse bias, the solar cell is in a reversed biased diode mode and only very small saturation current can pass through the diode. The reason for this unexpected initial large reverse current is due to the stored charges inside the solar cell. After the generated polarity is switched, the stored charges cannot disappear immediately and cause the junction voltage to remain positively biased. Then most of the $-V$ voltage from the generator has to drop across the resistor which makes the reverse current in the circuit approximately equal to $-V/R$ temporarily. The reverse current $-V/R$ will remain until all the stored excess electrons in the base region are recombined by the holes. Thereafter, the reverse bias diode behaviour of the solar cell takes place and only a very small reverse saturation current can pass through the solar cell and therefore most of the source voltage drops across the solar cell. The time T_{sd} taken for the stored charge in the solar cell to recombine is characterized by the storage delay time. This storage time is related to the lifetime of electrons through the transient equation as follows.

For an emitter heavily n doped solar cell, it is initially forward biased with a current I_f in the circuit. At time $t = 0$, the reverse bias from the generator makes the current in the circuit $-I_r$.

Solve equation 2.41 with Laplace transforms, with $i(t > 0) = I_r$ and $Q_n(0) = I_f\tau_n$

$$L\{i(t)\} = L\left\{\frac{Q_n(t)}{\tau_n}\right\} + L\left\{\frac{dQ_n(t)}{dt}\right\} \quad (2.42)$$

$$-\frac{I_r}{s} = \frac{Q_n(s)}{\tau_n} + sQ_n(s) - I_f\tau_n \quad (2.43)$$

$$Q_n(s) = \frac{I_f\tau_n}{s + 1/\tau_n} - \frac{I_r}{s(s + 1/\tau_n)} \quad (2.44)$$

Taking the inverse Laplace transform of the above equation, we get

$$Q_n(t) = I_f\tau_n e^{-t/\tau_n} + I_r\tau_n(e^{-t/\tau_n} - 1) = \tau_n[-I_r + (I_f + I_r)e^{-t/\tau_n}] \quad (2.45)$$

Assuming that $Q_n(t) = qAL_n\Delta n_p(t)$ from 2.40

$$\Delta n_p(t) = \frac{\tau_n}{qAL_n}[-I_r + (I_f + I_r)e^{-t/\tau_n}] \quad (2.46)$$

when $t = t_{sd}$, excess electrons $\Delta n_p(t)$ in the p region equals 0 and thus t_{sd} can be expressed as,

$$t_{sd} = \tau_n \ln \left[1 + \frac{I_f}{I_r} \right] [33] \quad (2.47)$$

The minority carrier lifetime τ_n in the p region can be calculated from the measured storage delay time.

Chapter 3

Discussion of Flexible Silicon Solar Cell

3.1 Performance

Fig. 3.1 and 3.2 show the top view and back view of a sample flexible silicon solar cell fabricated in the lab. The size of the sample is 1.82 cm^2 . There are four rows of solar cell die in the sample. The distance between two rows is 0.77mm. The distance between two solar cell die is 1.29mm. 14 square solar cell die (2.58mm by 2.58mm) in the figure were diced from commercial silicon solar cell(provided by ARISE Technology). All of them are connected in parallel with each other. Top electrodes of the solar cell die are interconnected through four copper wires which are finally connected together at one end. Bottom electrodes of the 14 solar cell die are also connected together by growing a copper film at the back side of the sample as shown in fig.3.2. The front and back electrodes are insulated from each other as shown by the transparent region between two electrode regions.

The electrical performance of this sample cell is investigated in a dark condition and one sun condition. In a dark condition, current passing through the sample is measured when a varying bias is applied to the flexible solar cell sample from -0.5 volts to 0.5 volts with 0.01 volts increments. The sample shows obvious diode rectifying behavior from fig. 3.3. In the forward bias, the sample allows large amount of current passing through. In the reverse bias, only a very small amount of thermally generated current can pass through the sample.

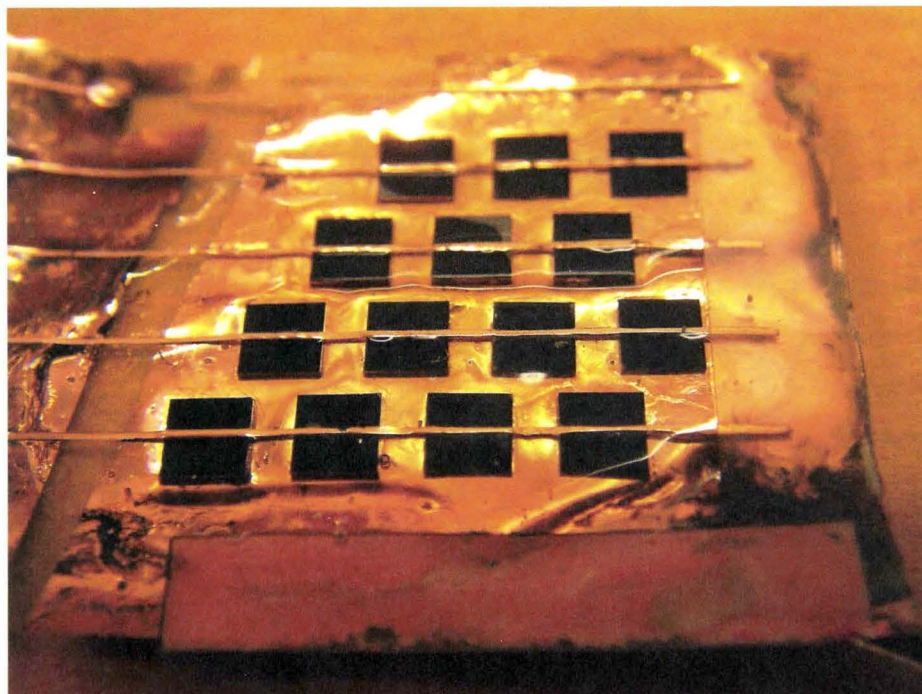


Figure 3.1: Front view of flexible silicon solar cell sample in this thesis



Figure 3.2: Backside view of flexible silicon solar cell sample in this thesis

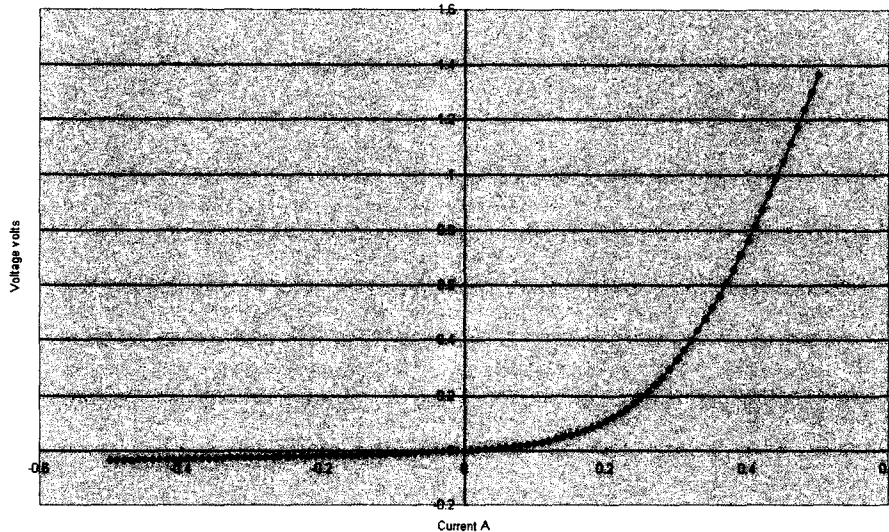


Figure 3.3: IV scan for the flexible solar cell sample in a dark condition

In the one sun illuminating condition, current passing through the sample is measured when a varying bias is applied to the flexible solar cell sample from -1 volts to 1 volts with 0.025 volts increments. Fig.3.4 shows electrical performance of the sample. From the I-V curve, the I-V fill factor, the short circuit current, open circuit voltage and conversion efficiency are found to be 50.34%, 32mA, 0.475 volts and 4.45% for an area of 4cm^2 respectively. The maximum output power of this sample is 8.09 mW. The area covered by 14 active silicon solar cell die is 51.34% of the total area. The actual cell efficiency is therefore almost twice the measured 4.45% value.

The performance of the whole sample is in fact the sum of performance of the 14 individual solar cell die. An aperture of the same size as the solar cell die was used to achieve light shining onto only one die under one sun condition. The IV performance for 14 solar cell die were individually measured. The corresponding curves are shown in fig.3.5. All 14 solar cell die can generate current. Their open circuit voltages are between 0.3 volts and 0.4 volts. Their short circuit currents are between 0.24 and 0.27 mA.

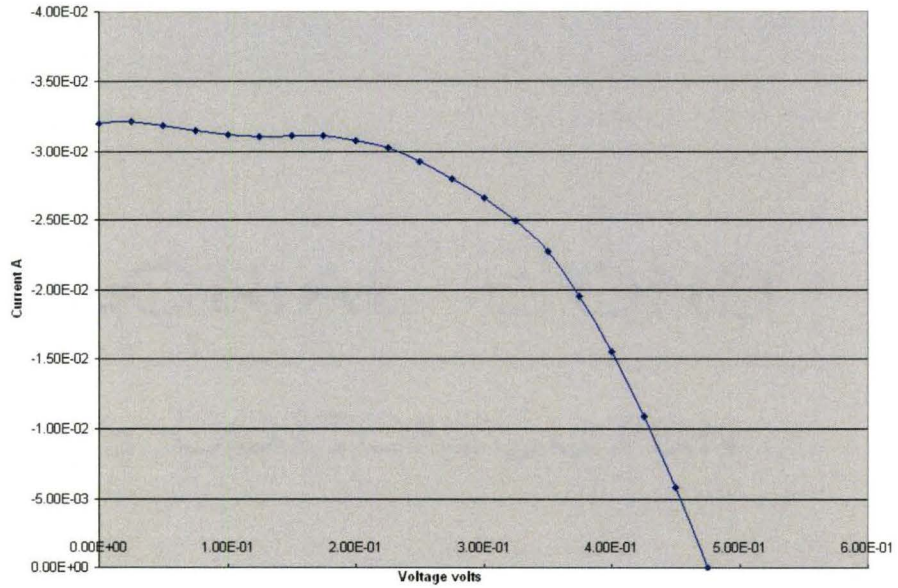


Figure 3.4: IV curve of a flexible silicon solar cell measured under one sun condition

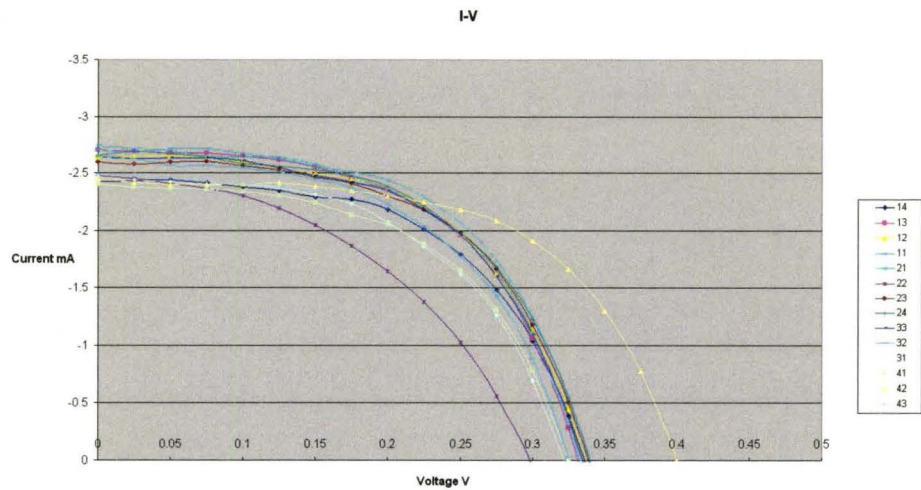


Figure 3.5: Performance of 14 solar cell die in the sample cell

3.2 Fabrication of flexible solar cell in this thesis

The flexible solar cell structure in this thesis is based on a method to interconnect LED chip arrays[41]. The detailed fabrication process to complete the flexible solar cell in this thesis is described below:

1. Dice square shape solar cell die from commercial solar cell using dicing saw.
2. Sputter copper thin film onto the hydrophilic side of a Tefzel film which is covered by a mask to define front electrode.
3. Apply solder flux onto the front copper electrode to remove the oxide layer on the copper electrodes.
4. Coat the copper electrodes using low melting alloy (melting temperature of the alloy of bismuth and tin is 140 Celsius).
5. Apply the same low melting alloy onto the top electrode of the solar cell die.
6. Pattern solar cell die onto a sticky layer (Gel Pack) to form arrays of solar cell die. Flip the sticky layer and align the top electrodes of the solar cell die with low melting alloy coated copper stripes on the Tefzel film.
7. Apply heat to the whole structure in step 6 on a hot plate up to 140 Celsius. Wait until the low melting alloy (LMA) melts between the copper electrodes on the Tefzel and the LMA on the solar cell die. Cool the structure to room temperature.
8. When the LMA is solidified, a conductive mechanical bonding is formed between top electrodes of the solar cell die and copper electrodes on the Tefzel.
9. Fill the space between solar cell die with an appropriate amount of epoxy.
10. Cure the epoxy between the die by placing the sample on a hot plate at 80 Celsius for one hour. The epoxy interconnects solar cell die so that they are secured

during bending. The epoxy layer also prevents forming short circuit between the top and bottom electrodes.

11. Isolate back-electrode and front electrode from one another. Sputter a 500nm copper thin film to cover the entire back side of the sample.

12. Remove the thin sticky tape which separates the front and back electrodes of the sample.

Chapter 4

Experiment and Discussion

4.1 Analysis of efficiency loss due to dicing process

4.1.1 Crystal structure of the test solar cell

In all the experimental sections, the test solar cells are provided by SunMaxx and the part number of the cell is 07-1200.

The crystal type of the test silicon solar cell has been identified to be polycrystalline silicon. X-ray diffraction was employed to identify its crystal properties. Two X-ray diagrams are compared. One diagram shows a mono-crystalline silicon material with [100] orientation. The other diagram indicates that the test sample does not have a mono-crystalline silicon structure.

The aluminium back electrode of a solar cell was removed and grains can be observed with an optical microscope. The crystal structure of the test sample shows polycrystalline characteristics. A picture of the grain structure is shown in fig.4.3 and the average grain size was measured by finding the mean chord length. The mean chord length is the reciprocal of the number of boundary intersection points per unit length[43]. For a 30 mm line at random across fig.4.3 the grain boundaries intersected are counted. By repeating this procedure 4 times, the number of counts are 4, 6, 4,

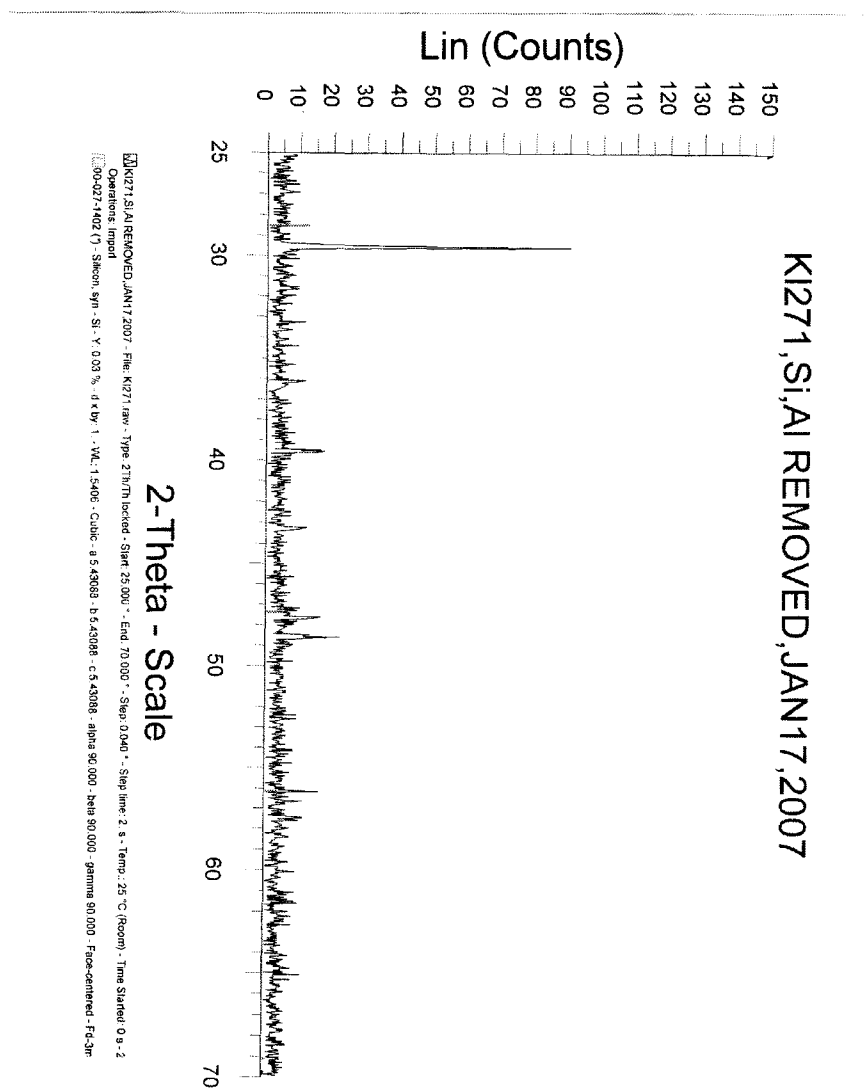


Figure 4.1: X-ray diffraction pattern of the test solar cell. The peak at 29.5 degree does not correspond to a silicon peak. It may be due to a Si-Br compound since P^+ doping is employed at the rear of the cell. Standard powder pattern for silicon is shown.

[42]

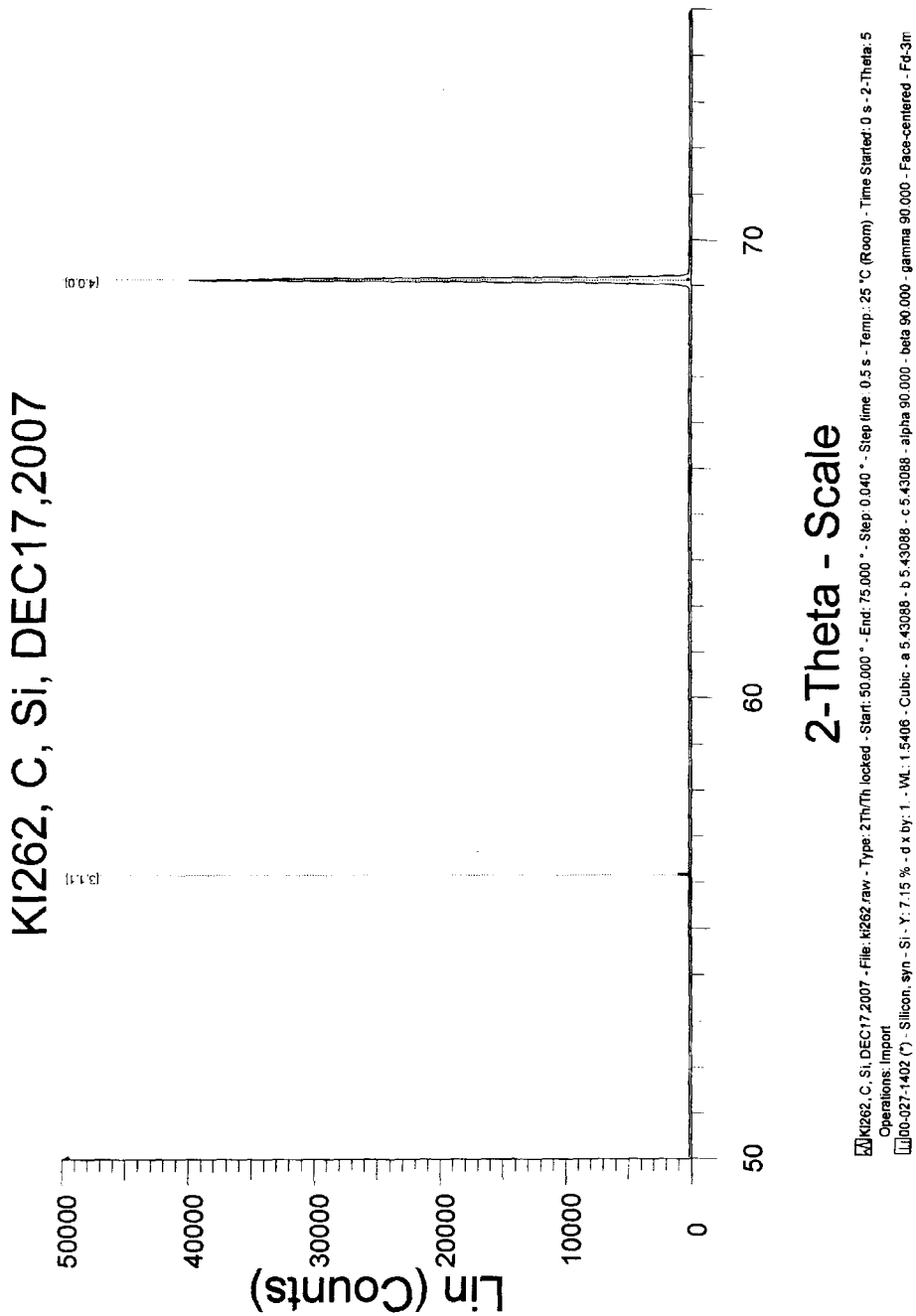


Figure 4.2: X-ray diffraction pattern of a monocrystalline silicon material with [100] crystal orientation. Standard powder pattern for Si.

[42]

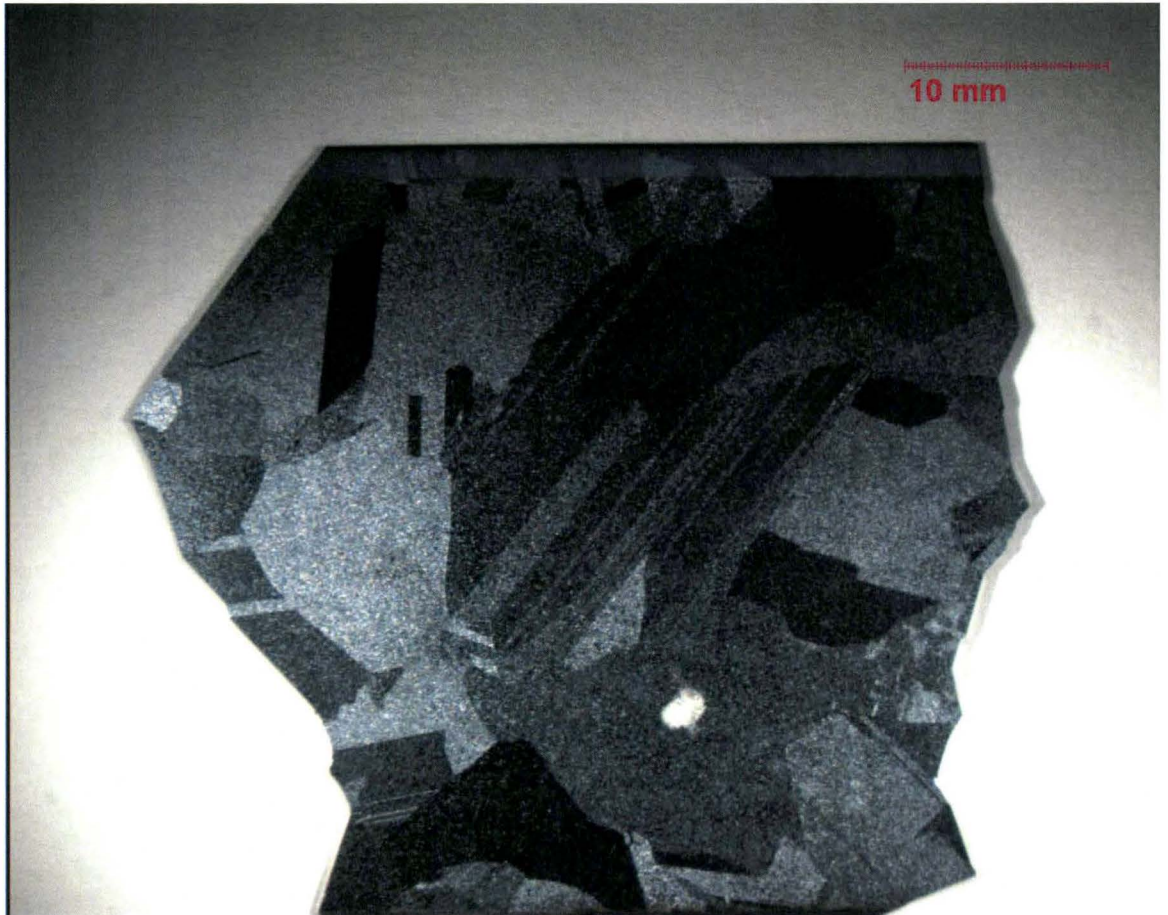


Figure 4.3: Grains of the test solar cell

3, and hence there are 17 counts for 120 mm. Therefore, the average grain size is estimated to be 7 mm.

4.1.2 Storage delay time measurement

The flexible solar cell structure get its solar cell dice by dicing a complete 6 inch by 6 inch commercial solar cell. Admittedly, dicing process introduces some efficiency loss from its original conversion efficiency, however, further investigation shows that efficiency loss may be controlled by choosing proper dicing methods. Different dicing methods may affect the conversion efficiency differently. An investigation of two dicing

methods was conducted to estimate which one may cause less efficiency loss. Solar cells are diced into 2.58mm by 2.58mm solar cell die from a complete commercial solar cell. One type of these solar cell die was obtained by dicing the cell from the front surface completely through the cell. Another other method is to dice the cell from the back surface partially and then cleave through the cells. These two dicing methods are shown in fig.4.4 and fig.4.5

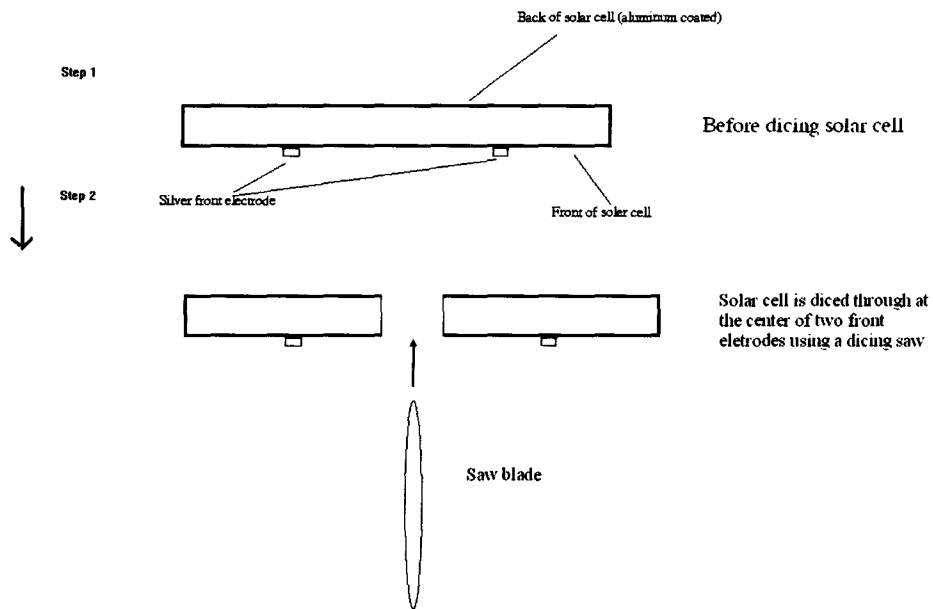


Figure 4.4: A solar cell is diced through

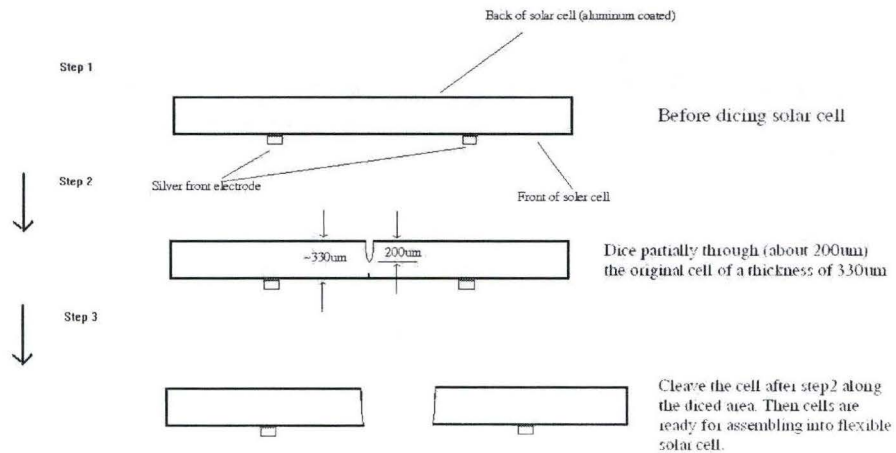


Figure 4.5: A solar cell is partially diced and then cleaved through

For test cells which were fabricated by dicing all the way through the original 6 inch by 6 inch solar cell using a dicing saw, the measured conversion efficiencies are all around 8%. This means that there was saw-induced damage and degradation to the silicon cells, which started out at a conversion efficiency of 15% before dicing. For the cells which were fabricated by partially dicing the original 6 inch by 6 inch solar cell from the back side (the back side is aluminum coated) to a depth of approximately 200 microns and then cleaved into individual cells, the measured conversion efficiency of the cells is close to the conversion efficiency of the original un-diced solar cell, which is 15%. The total thickness of the complete solar cell is about 330 microns. A preferred method of dicing is to dice a solar cell partially through and then cleave it into individual die.

Efficiency loss from different dicing methods can be also compared through examination of the carrier lifetime of two types of die. Minority carrier lifetime of these

two types of cell die may be obtained from storage charge delay time measurement. A correlation between different dicing methods and conversion efficiency can be derived from this analysis by comparing measured excess electron lifetime in the p region. The storage charge delay time of solar cell die diced partially and then cleaved through and solar cell die diced all the way through are compared.

In the circuit, a wave function generator is connected to a solar cell which is also in series with a resistor R of 100 ohms. A square wave is generated from the function generator. The voltage at point A and the voltage at point B, as shown in fig.4.6 and the solar cell are measured and compared.

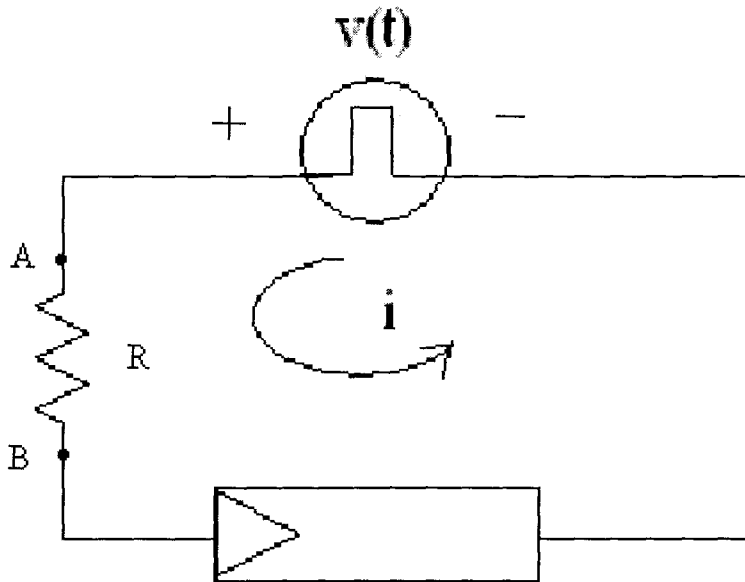


Figure 4.6: A schematic diagram of storage charge delay time measurement setup

The voltages at points A and B were measured as a function of time as shown in fig. 4.7

From fig.4.7, as the polarity of the function generator is switched, the measured voltage at point A immediately switches from a positive value to a negative value. However, this is not the case for the voltage at point B. When the polarity is switched,

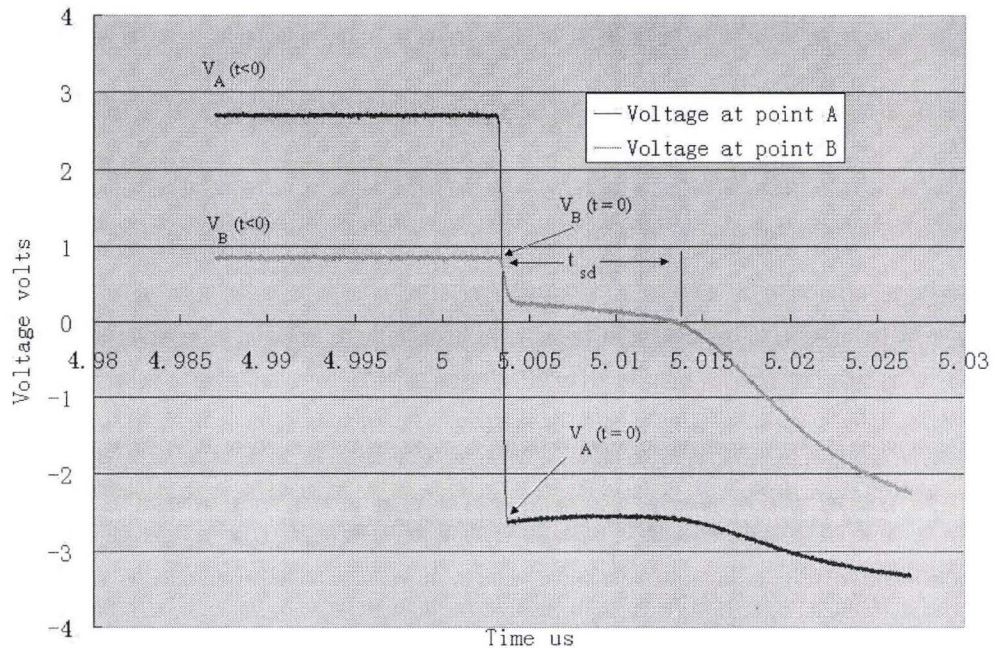


Figure 4.7: A plot of measurement of storage delay time from measured voltages at point A and B with respect to time for one sample cell

the voltage at point B remains a positive value for a period of time defined by storage delay time t_{sd} . The delay of change of voltage is due to the remaining minority carrier electrons which cannot disappear immediately in the n region. It takes t_{sd} for the electrons to recombine with the holes. Therefore, the experimental result is consistent with theory stated at section 2.5.

According to equation 2.47 in the theory part of Storage Delay Time,

$$t_{sd} = \tau_n \ln \left[1 + \frac{I_f}{I_r} \right]$$

The lifetime of excess electrons τ_n can be obtained in terms of the storage delay time if t_{sd} is known. t_{sd} can be measured directly from fig.4.7 where it is equal to the

time taken for the voltage at point B to decline to zero after the generator switches its polarity. In equation 2.47,

$$I_f = \frac{V_A(t < 0) - V_B(t < 0)}{R} \quad (4.1)$$

$$I_r = \frac{V_B(= 0) - V_A(t = 0)}{R} \quad (4.2)$$

The minority carrier lifetime in the p region of the solar cell can be obtained through the following equation:

$$\tau_n = \frac{t_{sd}}{\ln \left[1 + \frac{I_f}{I_r} \right]} \quad (4.3)$$

By measuring t_{sd} , I_f and I_r from storage delay time experiment, and applying equation 4.3, excess electron lifetime in the p region of solar cells die may be obtained.

The sample mean value of the lifetime for both two data sets can be obtained by

$$\bar{x} = \frac{1}{N} \sum_{i=1}^N x_i = \frac{x_1 + x_1 + x_3 \cdots + x_N}{N} \quad (4.4)$$

and the corresponding sample standard deviation using

$$s = \sqrt{\frac{1}{N-1} \sum_{i=1}^N (x_i - \bar{x})^2} \quad (4.5)$$

The storage delay time of one set of 29 silicon solar cell die (2.58mm by 2.58mm, diced all the way through) may now be determined to investigate the corresponding dicing method's effect on the carrier lifetime of the excess electrons in the p region. The calculated lifetimes for these 29 cell die are shown in fig.4.8.

As shown in fig.4.8, the obtained excess electron lifetime ranges between $0.89\mu s$ and $5.59\mu s$. The sample mean lifetime \bar{x} of these 29 cell die is $3.046\mu s$ and the sample standard deviation s is $1.326\mu s$.

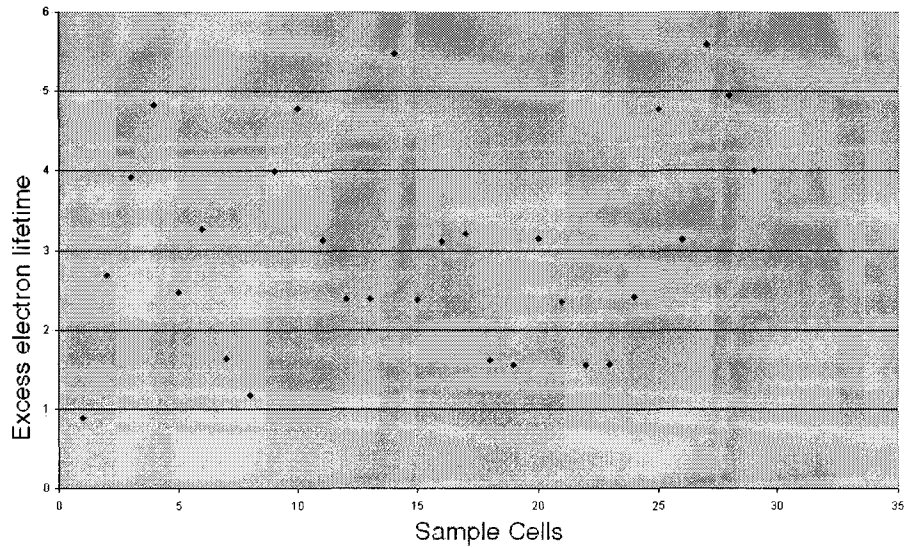


Figure 4.8: The excess electron lifetime of 29 cell die diced all the way through

The storage delay time of 15 silicon solar cell die (2.58mm by 2.58mm, diced partially from back then cleaved through) was measured to investigate the corresponding dicing method's effect on the carrier lifetime of the excess electrons in the p region. The calculated lifetime for these 15 cells are shown in fig.4.9.

As shown in fig.4.9, the obtained excess electron lifetime ranges between $10.11\mu s$ and $14.19\mu s$. The sample mean lifetime \bar{x} of these 15 cell die is $12.395\mu s$ and the sample standard deviation s is $1.325\mu s$.

Since all the lifetime measurements of samples in each data set can be considered identical in their own set, a Gaussian distribution can be employed to analyze and compare the two data sets. According to Gaussian distribution, the probability density distribution is

$$p(x, \sigma, \mu) = \frac{1}{\sqrt{2\pi}\sigma} \exp\left(-\frac{(x - \mu)^2}{2\sigma^2}\right) \quad (4.6)$$

The mean value μ and standard deviation σ are estimated by sample mean value \bar{x} and sample standard deviation s .

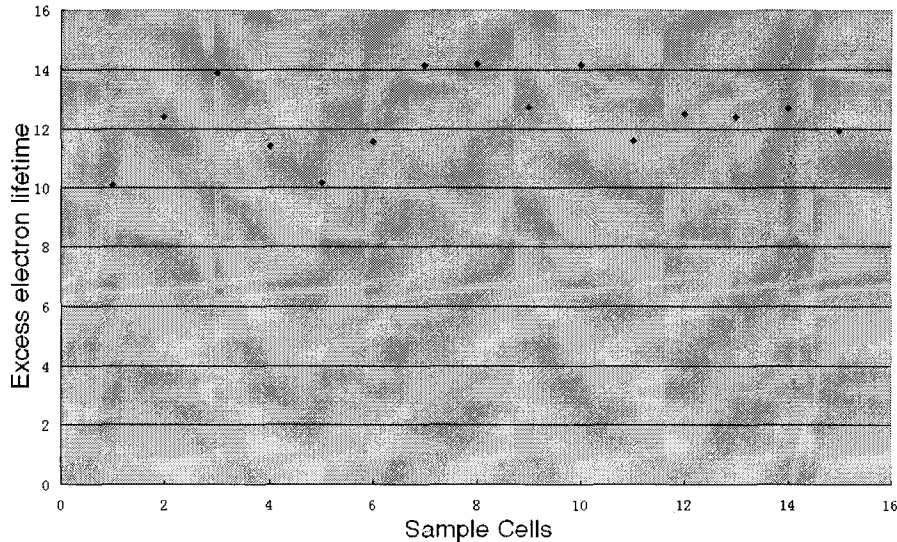


Figure 4.9: The excess electron lifetime of 15 cells diced partially and then cleaved through

A plot of the Gaussian distribution of these two sets of data is shown in figure 4.10. The green curve of 15 cell die is on the right side of the blue curve of 29 cell die. This can be explained in a way that the 29 diced-through die have a longer average excess carrier lifetime compared to that of the 15 partially-diced-through cells. The variation of the 15 cell die is close to that of the 29 cell die. The ratio of the sample standard deviation and the sample mean value $\frac{s}{\bar{x}}$ gives the relative fluctuation of the data set. The data set of 29 cell die has a relative fluctuation of 43.49% and the data set of 15 cell die has a relative fluctuation of 10.68%. Although the sample standard deviation of the two data sets are close to one another, the large difference of relative fluctuations illustrates the fact that the 29 cell die has a wider spread of lifetime values. This can be physically explained by the fact that more defects are introduced into the sample cells through the fully-dicing-through method. As a result of this dicing method, a smaller and wider spread in excess electrons lifetime was observed and this indicates a lower conversion efficiency.

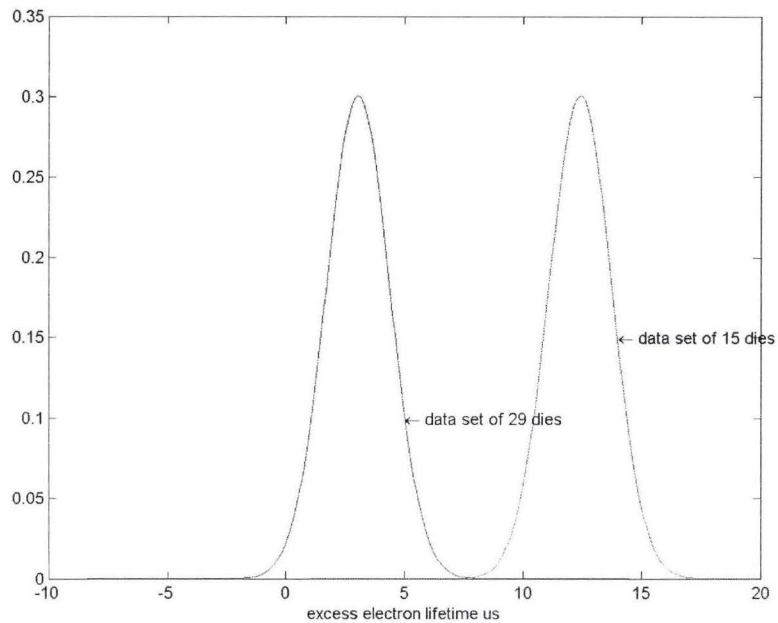


Figure 4.10: Two Gaussian distributions for two different diced sample data. The blue curve represents 29 cells and the green curve represents 15 cells

From the analysis of Gaussian Distribution of the two data sets, it is found that die will have less efficiency loss if diced partially and then cleaved through.

Efficiency loss after dicing process may result from two factors. One of them being the presence of parallel shunt resistance at the damaged edges, the other one being the high recombination current due to the defects at the edges of the die.

4.1.3 Light beam induced current scanning

Light beam induced current(LBIC) scanning technique[44,45] is employed to detect the spatial defects of solar cell die which have been diced. The attention will be focused on the vicinity of the edge of the solar cell die. Since the solar cell is mechanically diced, many defects are introduced to the edge region of the solar cell die. By measuring the open circuit voltage V_{oc} , short circuit current I_{sc} and maximum power P_{max} near the edge, information on the degree of damage due to the dicing process can be estimated.

Laser Beam Probe: An unpulsed 635nm He-Ne laser beam is focused down to $15 \pm 2\mu\text{m}$ diameter size. A microscope objective lens with a working distance of 1.4mm from the objective lens surface was used to concentrate the HeNe laser light beam onto the surface of the cell being investigated. The power out of the laser beam after passing the objective lens was measured to be 0.715mW.

The solar cell die were mounted on a three dimensional stage. One dimension of the three stages is on a motorized linear stage (UTM 100 pp1hL) so that the solar cell can move perpendicularly relative to the incident laser beam. The minimum stepping distance between each measurement was set to be $20\mu\text{m}$.

An equivalent circuit of light beam induced current scanning over a solar cell is shown in fig.4.11[44].

Fig.4.11 shows the equivalent circuit of a spot illuminated solar cell. The circuit is a combination of an illuminated area of a solar cell and the unilluminated bulk part of the solar cell. R_{series} and R_{shunt} are the series and parallel(shunt) resistance of the illuminated area. R'_{series} and R'_{shunt} are the series and parallel or shunt resistance of the unilluminated bulk area of the solar cell. The current flowing through the unilluminated area of the solar cell consists of the dark current through the bulk part

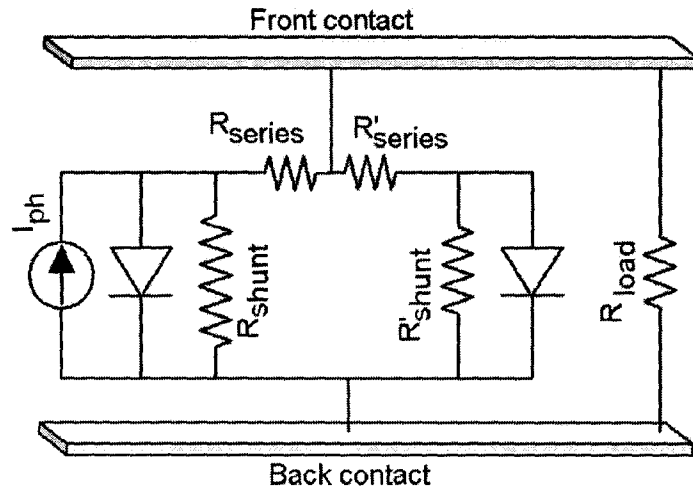


Figure 4.11: An equivalent circuit of light spot on a solar cell

and the current through the R'_{shunt} parallel resistance[44,45].

Data acquisition and the traveling stage control was programmed using *LabView*^R.

Equipment setup

1. Aligning the experiment: Mount the microscope lens on a three axis micrometer stage and place the lens in the path of the laser beam. Place a power meter sensor behind the microscope lens and change the position of the lens using the micrometers until the power meter registers the highest value.
2. Remove the power meter and replace with a three axis stage containing the sample solar cell. Adjust the position of the cell so that it is at the focal point of the lens (in our setup we found it to be 1.4mm for a $15 \pm 2\mu\text{m}$ spot size).
3. Using the two degrees of freedom which control the stage motion perpendicular to the laser beam, set the stop to an edge of the solar cell. To assure that the spot is not on the cell, the open circuit voltage for the cell can be measured (in a dark room).
4. When the edge is found take an I-V curve measurement for a base value.
5. Move the stage in one dimension a set interval and measure the I-V curve again until the whole cell has been scanned.
6. When the I-V curves are measured the open circuit voltage V_{oc} , short circuit

current I_{sc} and maximum power P_{max} can be calculated for each point.

7. Graphing this data gives a profile of the cells characteristics as a function of position.

The setup of equipment is shown in fig. 4.12

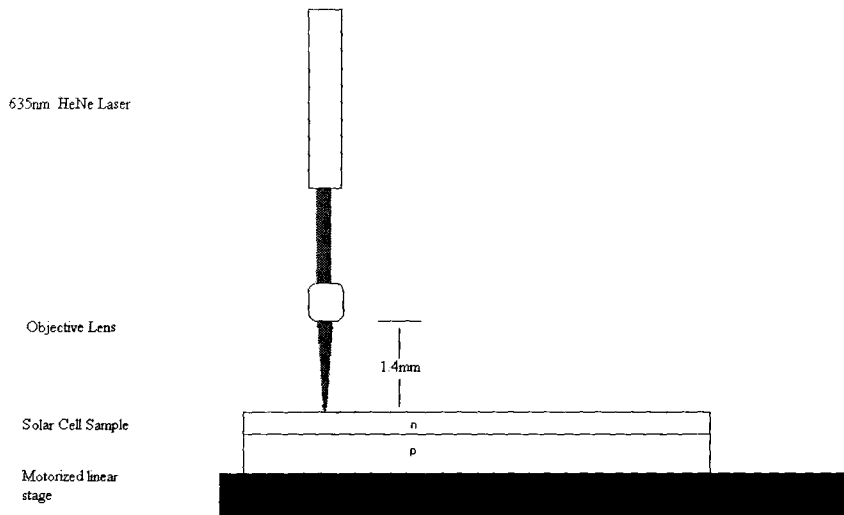


Figure 4.12: A schematic diagram of light beam induced current (LBIC) experiment setup

The laser beam is focused onto the front surface of the solar cell (the surface which faces the light source when the device is in operation). The I-V curve of the cell was recorded as a function of laser beam position on the surface of the solar cell die. Key parameters, such as open circuit voltage V_{oc} , short circuit current I_{sc} and maximum power P_{max} can be derived from the I-V curves of every position of the solar cell die surface scanned by the laser beam. The horizontal measurement was done using a motorized traveling stage with $20\mu\text{m}$ step for each measurement. The vertical measurement was done by manually adjusting a microstage with $20\mu\text{m}$ step for each measurement. Fig. 4.13 and 4.14 illustrate surface maps of V_{oc} of a solar cell die which was diced partially and cleaved through. The scale of V_{oc} is expressed in

the color bar in fig.4.13 and 4.14 where the deep red regions indicate the active cell surface and the yellow regions exhibit the outside of the solar cell surface. The length of the test solar cell die (about 2.6mm) can be obtained from the horizontal axes of the two diagrams. This value is consistent with the width of the solar cell die. The measurements along the vertical direction (about 400um in that direction) in fig.4.13 and 4.14 cover only part of the solar cell surface. Since the cell was diced partially and then cleaved through, the edges of the cell exhibit rough surface topograph as indicated by the large variation of V_{oc} on the edges of the solar cell die. The large uneven distribution of V_{oc} is from the damaged edge due to the dicing and cleaving process. Another feature in the two figures is the big drop of V_{oc} on the surface plane. Since the front contact fingers (silver electrodes) prevent laser beam from penetrating into bulk region of the cell to generate electron-hole pairs, nearly zero V_{oc} is shown in fig.4.13 and 4.14. From the width of the dropped voltage in figure 4.13, the width of the front contact fingers can be measured and is found to be about 120um which is also consistent with a contact finger width measurement using a microscope.

The 2.58mm by 2.58mm solar cell die were diced from a complete commercial solar cell using a dicing saw. The edges of the solar cell die which were diced partially and then cleaved through are rough and obvious transition edges can be observed from fig.4.14. It is worth noticing that the horizontal edge from fig.4.14 appears not perpendicular to the two vertical edges. This is because the horizontal and vertical units are not in the same scale. Since the horizontal measurement was scanned using a motorized stage and the vertical measurement was scanned manually, there are more data points along the horizontal direction than in the vertical direction. Although the measurements of both directions have the same 20 μm step between each scan, visually the vertical 20 μm is much longer than the 20 μm in the horizontal direction.

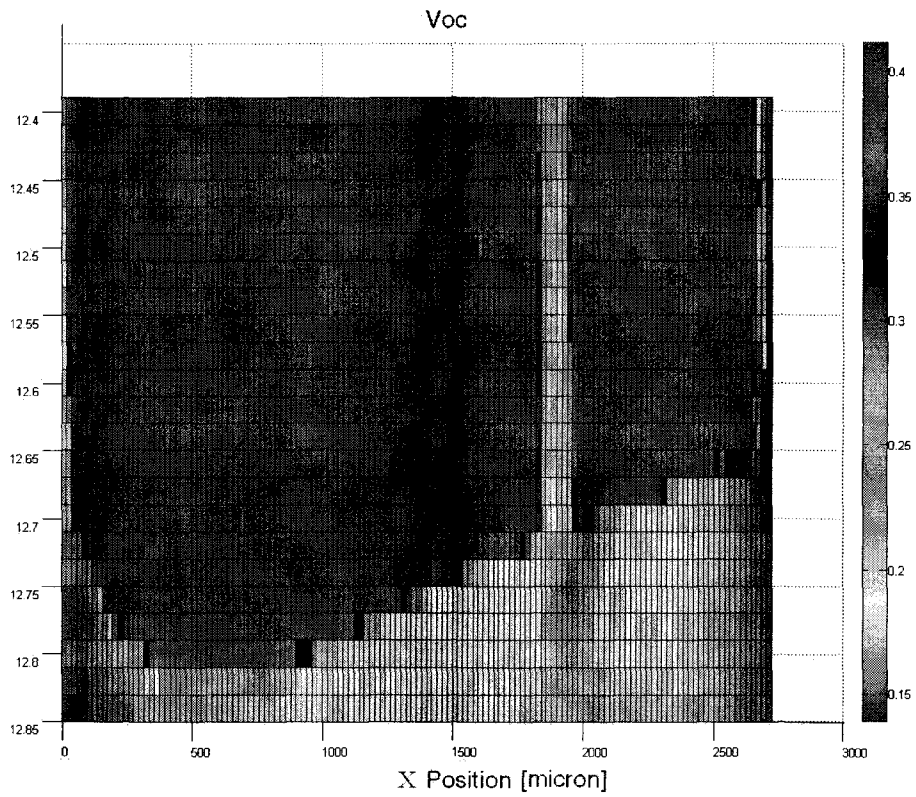


Figure 4.13: Two dimensional view of open circuit voltage at each point of a solar cell surface which was diced partially and then cleaved through

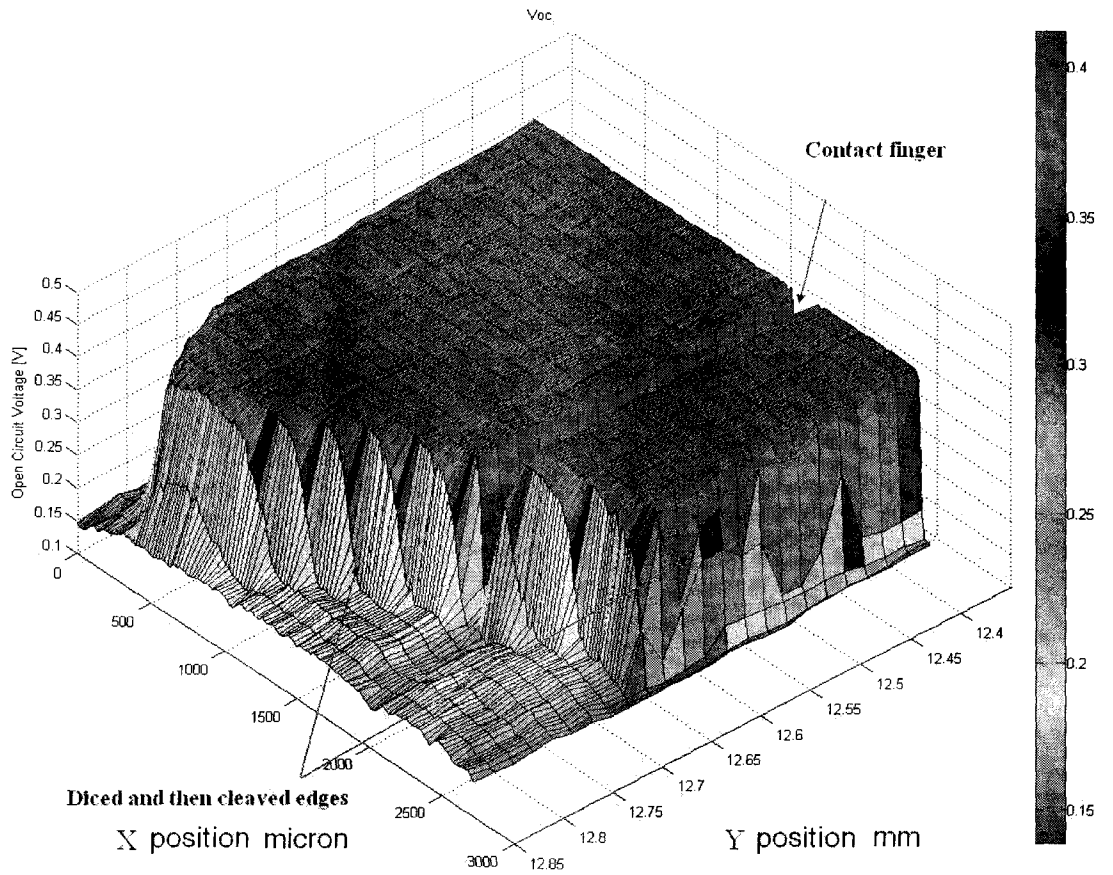


Figure 4.14: Three dimensional view of open circuit voltage at each point of a solar cell surface which was diced partially and then cleaved through

The edges of the solar cell die which were diced fully through are sharp and flat. The sharp edges can be seen from fig.4.17.

The performance of the same solar cell in terms of short circuit current and maximum output power versus laser beam positions is graphed in figures 4.15 and 4.16. The figure of I_{sc} shows a rougher surface plane compared with the V_{oc} surface plane. The reason for this may be that when the contact finger of the solar cell die is under no bias to measure I_{sc} , the amount of current that reaches the contact fingers can be affected by local R_{series} at the illuminated p-n junction region in fig.4.11. Larger R_{series} values at the illuminated p-n junction region will yield smaller I_{sc} values. The large R_{series} can result from material defects of the solar cell and also from any other factors which may lower incident light intensity such as dust particles on the surface, and variations in the antireflection coating [44]. For the unilluminated cell surface, the current passing through the solar cell can be considered as dark current which is the sum of recombination current and shunt current. Since the bulk unilluminated area of the cell is much larger than that of the illuminated light spot, the resistance and recombination characteristics of the bulk region of the cell do not vary with the position of the light beam. Figures of I_{sc} may better indicate its characteristics such as the defect level, surface condition and etc., of a solar cell at a local region illuminated by the laser beam.

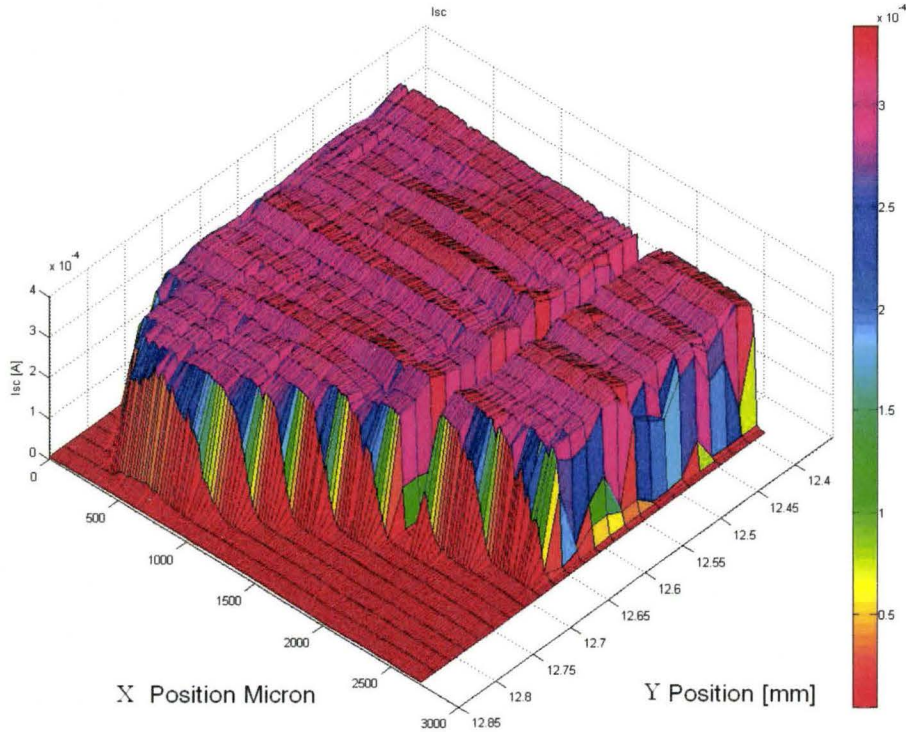


Figure 4.15: Three dimensional view of I_{sc} short circuit current at each point of a solar cell surface which was diced partially and then cleaved through

The cells which were diced partially through have sharper edge transitions since the edge surface is smoother than that of the cells which were diced partially and then cleaved through. Fig.4.17,4.18 and 4.19 exhibit the V_{oc} , I_{sc} and P_{max} characteristics as a function of the laser beam position on a cell surface. V_{oc} , I_{sc} and P_{max} are around 0.3mA, 0.5V and 0.1mW respectively. Since the incident laser beam intensity is 0.715mW, the conversion efficiency for this intensity is 14%. Since the laser is focused to a spot size of $15 \mu\text{m}$ in diameter, its intensity on the surface of the test solar cell is about 10,000 times higher comparing to light intensity at one sun condition. Concerns of overheating in the test cell may be arisen. However, because the light spot is very small, the heat can easily be conducted to the surrounding unilluminated

area. One method to eliminate this overheating problem is to use a pulse laser so that the laser beam is not continually shining on the test cell.

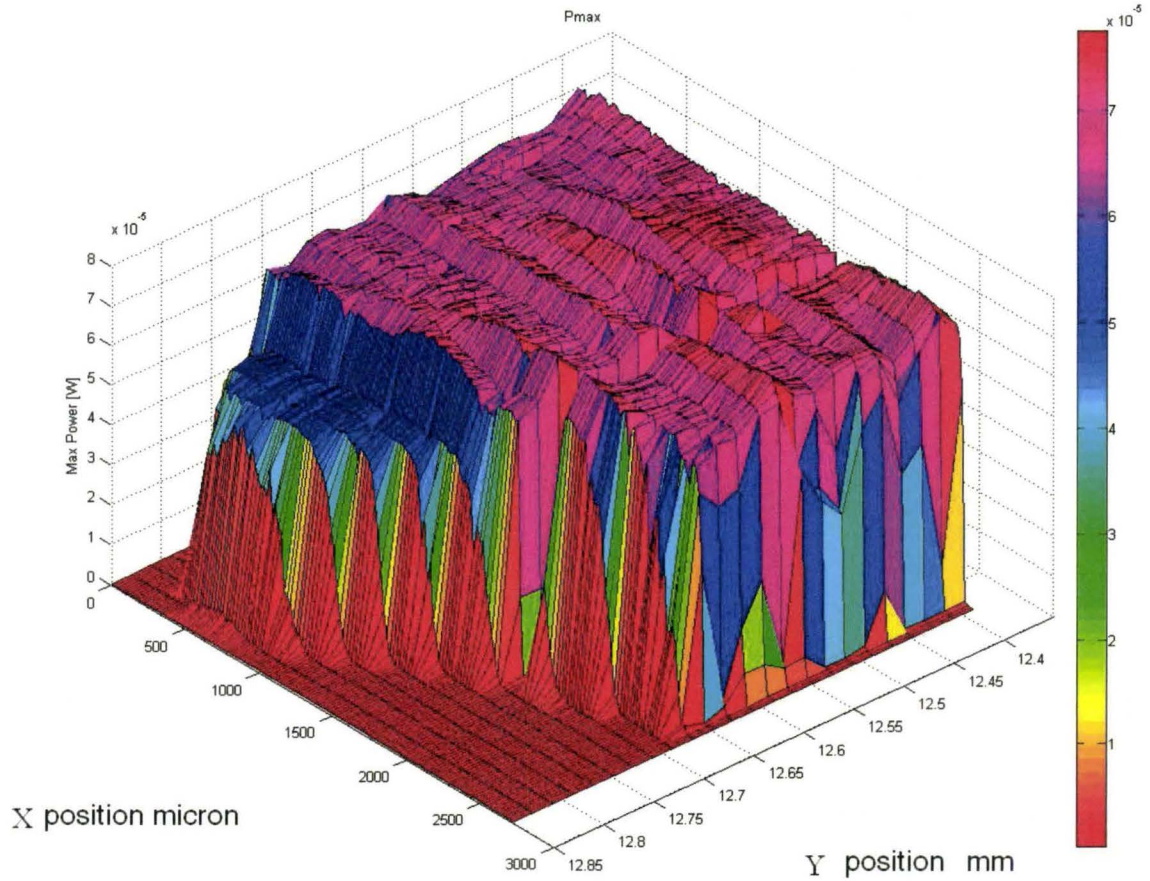


Figure 4.16: Three dimensional view of P_{max} at each point of a solar cell surface which was diced partially and then cleaved through

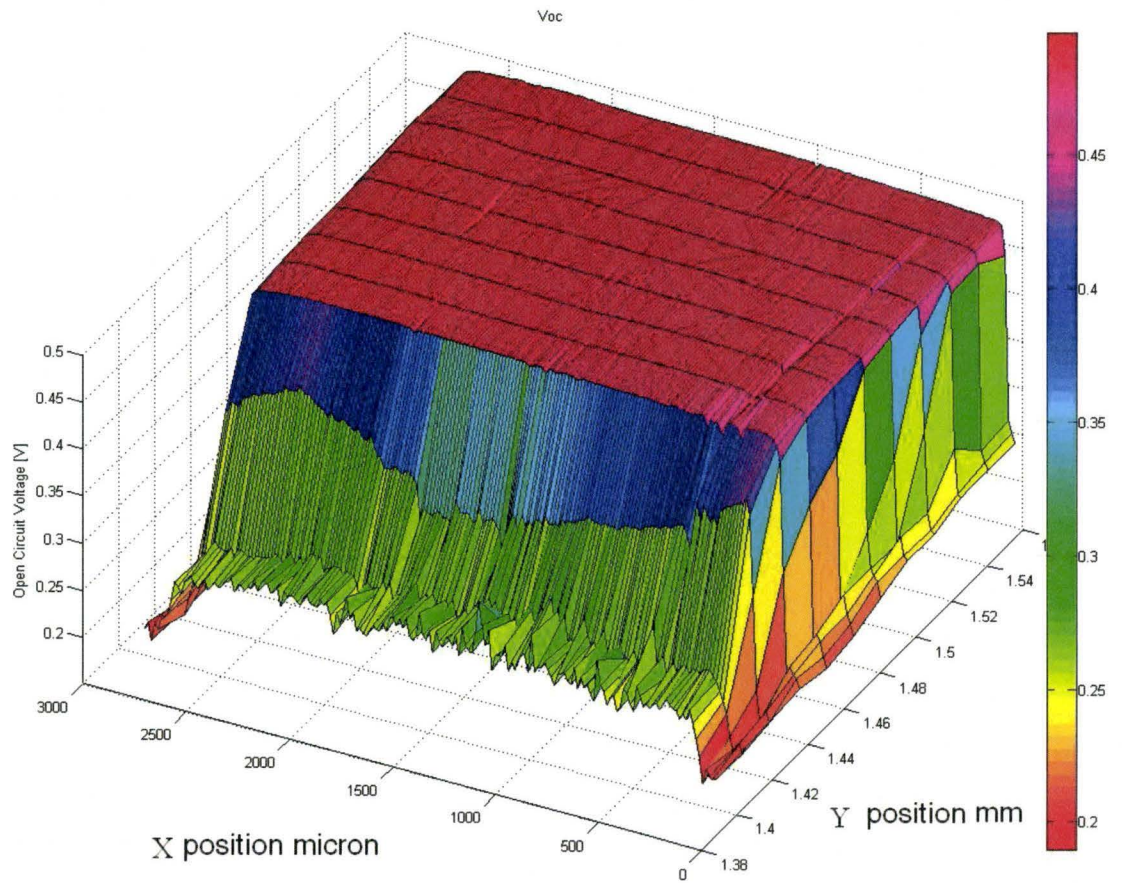


Figure 4.17: Three dimensional view of V_{oc} for a solar cell which was diced through

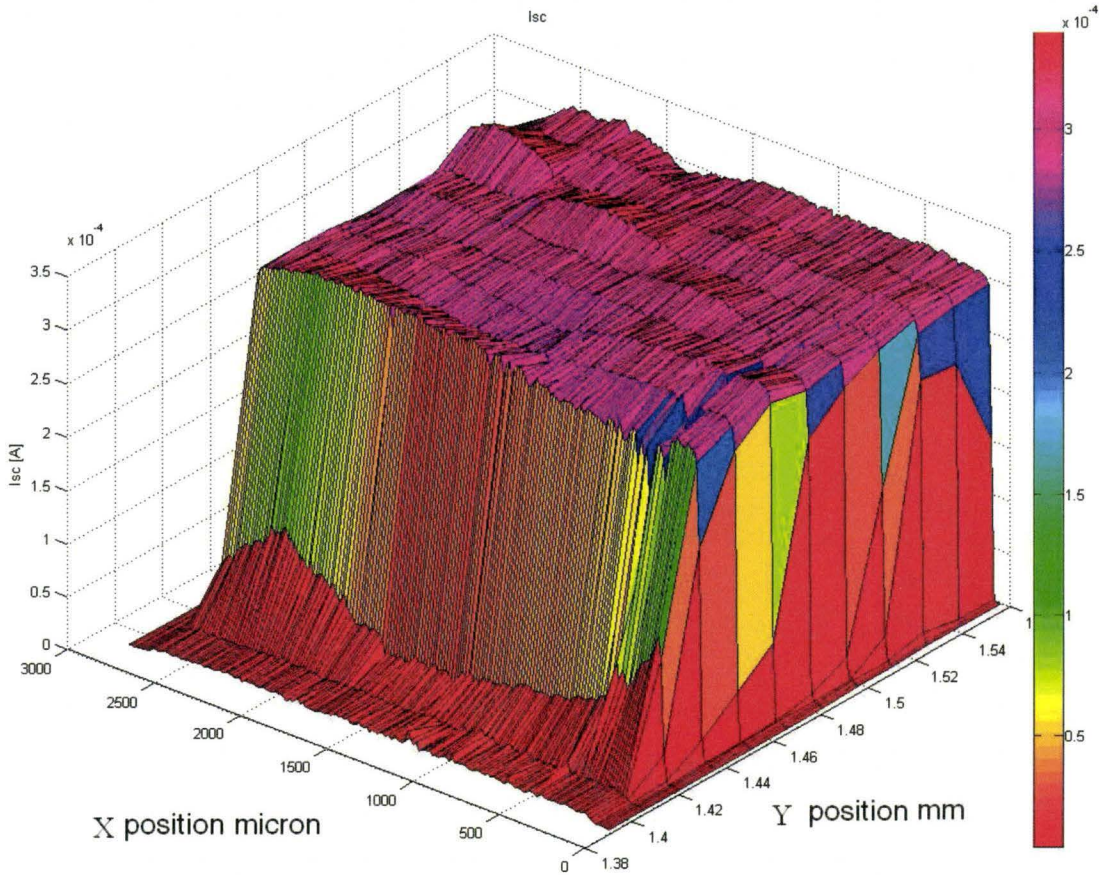


Figure 4.18: Three dimensional view of I_{sc} for a solar cell which was diced through

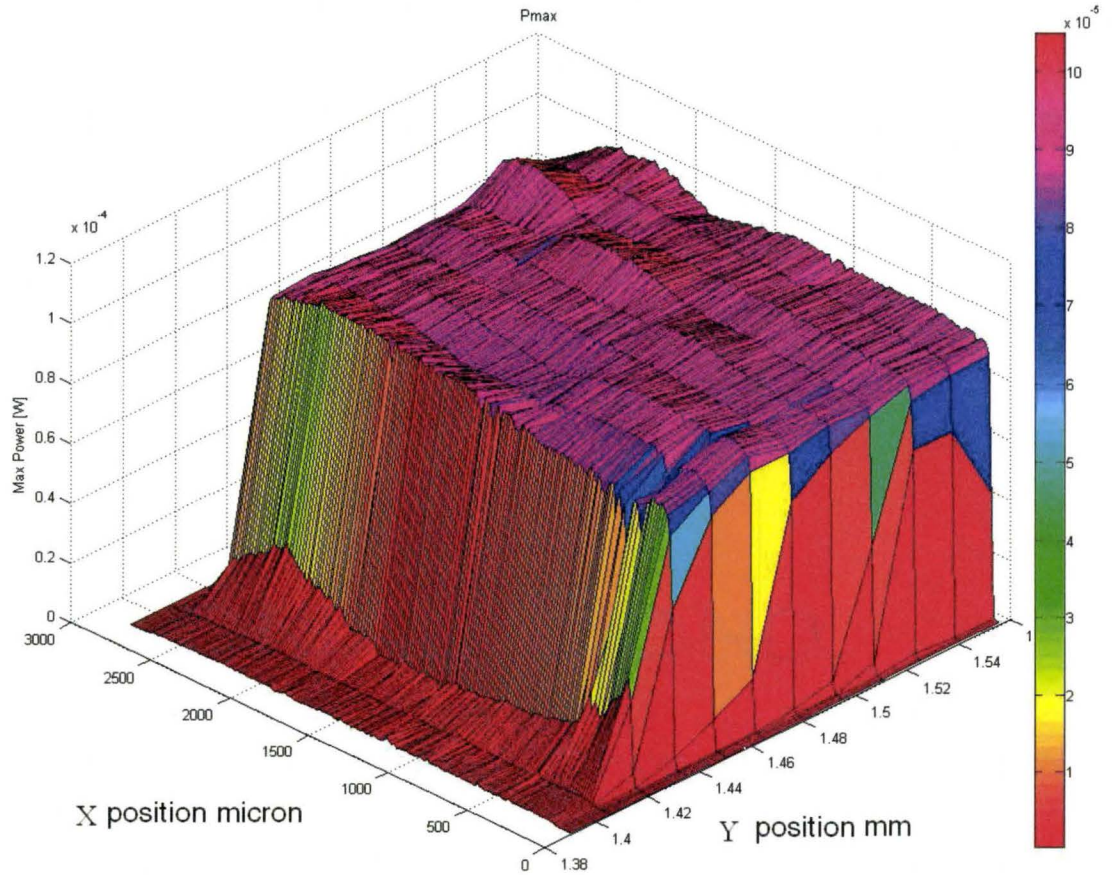


Figure 4.19: Three dimensional view of P_{max} for a solar cell which was diced through

4.1.4 Traveling light spot diffusion length measurement

Lifetimes of carriers may be obtained through a "traveling light spot" from diffusion length measurement. An unpulsed HeNe laser at 635nm is focused down to a beam of a diameter $15 \pm 2 \mu\text{m}$ using an objective lens (X 25). The power of the focused laser beam is measured to be 0.715mW. A 2.58mm by 2.58mm solar cell die is mounted on a traveling stage UTM 100 pp1hL . The laser beam is focused onto the edge of the test solar cell die and scanned across the p-n junction with steps of $3 \mu\text{m}$ as shown in fig. 4.20 and 4.21. The test solar cell die is connected with Keithley Source Measurement Unit 238 to take readings of the I-V characteristics of the solar cell die with respect to the beam position to the junction. The automatic measurement takes place at each position of the laser beam across the p-n junction.

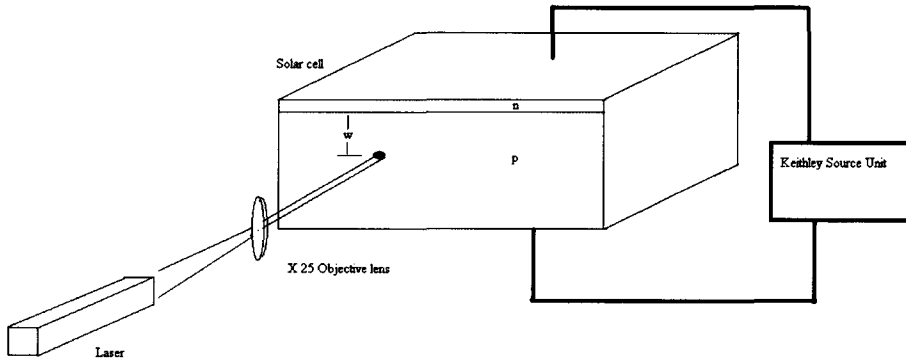


Figure 4.20: Schematic diagram of the traveling light spot diffusion length measurement

As shown in fig. 4.21, the diffusion length of a solar cell is measured by applying a focused laser beam onto the edge of the solar cell. The short circuit current is measured as a function of the laser spot position on the edge of the cell.

According to equation 2.8:

$$I_{sc} = C\phi_o \exp(-w/L_n)$$

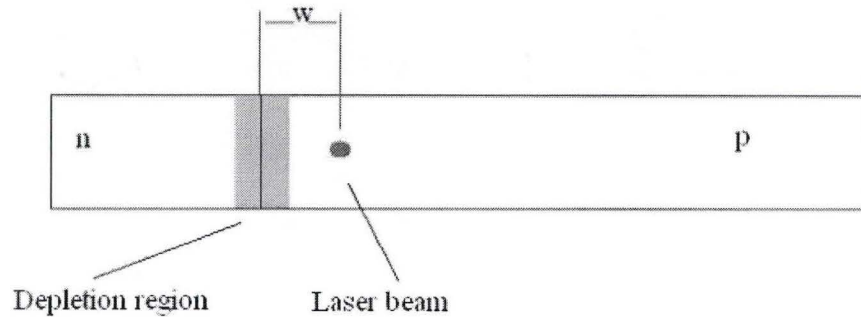


Figure 4.21: Schematic diagram of the traveling light spot diffusion length measurement

Where:

w represents the distance between the light beam and the junction

ϕ_o represents the incident laser beam intensity

L_n represents the diffusion length of excess electrons in the p region

I_{sc} represents the measured short circuit current from the solar cell die.

Short circuit current in equation 2.8 may be formulated by the product of a proportionality constant, incident light intensity and a spacial exponential decay term. I_{sc} is also a function of distance between the light beam and the junction. Both I_{sc} and w can be measured from the this experiment.

The exponential term in the equation accounts for the exponential decay of the excess charge carriers. The excess charge carriers generated at the illuminated spot diffuse to the junction and these charges then are swept across the junction by the electric field existing in the depletion region. Therefore, only can the charge carriers, which are not recombined during the diffusion and successfully reach the junction, contribute to the short circuit current. The number of these charges is governed by the product of the exponential term and the total charge generated by the laser beam. In the exponential term $\exp(-w/L)$, w is the distance between the laser beam and the junction. L is the minority carrier diffusion length which is to be obtained

through this experiment. Short circuit current will vary with the change of spacing w between the laser beam and junction. The closer the laser beam is to the junction, the larger the short circuit current becomes.

Theoretically, in the p region of a solar cell, there exists a linear relation for $\ln(I_{sc})$ and x . By taking the natural logarithm on both sides of the equation 2.8, and then taking the first derivative with respect to w , the diffusion length L of excess electrons in the P region may be obtained as 2.11

$$L_n = -\left(\frac{d \ln I_{sc}}{dw}\right)^{-1}$$

[34]

The laser beam is moved across the p-n junction from the n region to the p region with steps of $3\mu\text{m}$ by relatively moving the solar cell die on the traveling stage. The corresponding short circuit current is measured at each step and a relationship between $\ln I_{sc}$ and the corresponding distance to the junction w is plotted.

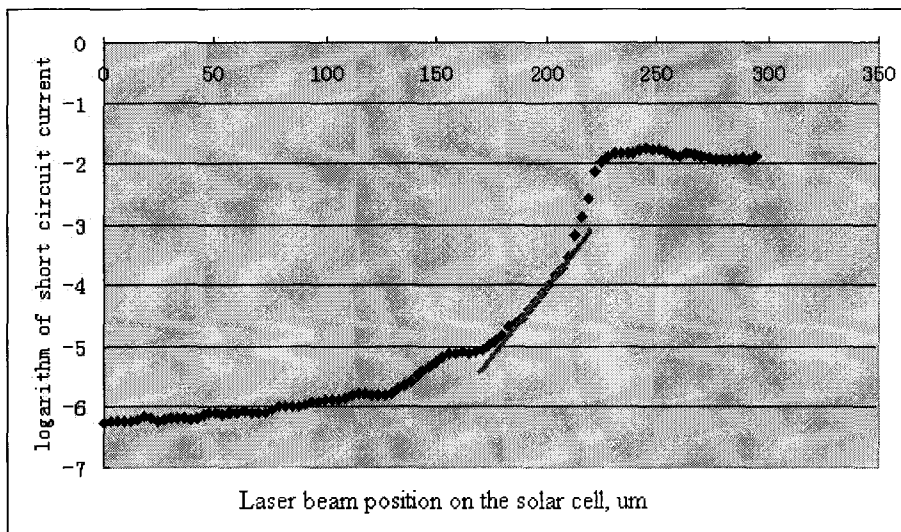


Figure 4.22: Logarithm of short-circuit current as a function of laser spot position.

If the laser light spot is scanned from the top surface of the solar cell across the junction, from fig.4.22, the I_{sc} graphs will start with a flat line, and then the curve

declines. This observation supports the fact that the light spot is initially on the surface and then gradually moves to the edge of the cell. Therefore, the flat part of the curve should not be considered part of the I_{sc} generated from the junction and also the first 5 or 6 points along should not be considered as the I_{sc} generated from the junction since the light spot diameter has a size of about 15 μm and the step size is about 3 μm ; hence the first 5 light spots are only partially on the junction. The slope of the I_{sc} can be approximated from the straight line shown in fig.4.22. The calculated diffusion length from the slope using equation 2.11 is 28 μm . The diffusion length of many other cells which are either partially diced and then cleaved through or diced completely through are also measured by this traveling light spot methods. The obtained diffusion lengths of these measurements are all within the range from 20 μm to 30 μm .

From a measurement of storage delay time (see section 4.1.1 for excess electron lifetime in the p region), the calculated average excess electron lifetime is about 12.4 μs for the cells which are diced partially and then cleaved through. If the minority carrier diffusion constant is 40 cm^2s^{-1} [3], the diffusion length of excess electrons in the p region can be obtained through the well-known equation

$$L = \sqrt{D\tau} \quad (4.7)$$

Then L is equal to 222 μm .

There are two reasons for this large deviation of diffusion length between two experimental results. First, the surface damage due to the dicing process strongly changes the result of the traveling spot measurement which very much relies on the surface condition of the test sample. Second, surface recombination has a large influence on traveling light spot diffusion length measurement .

Two more experimental figures are shown below.

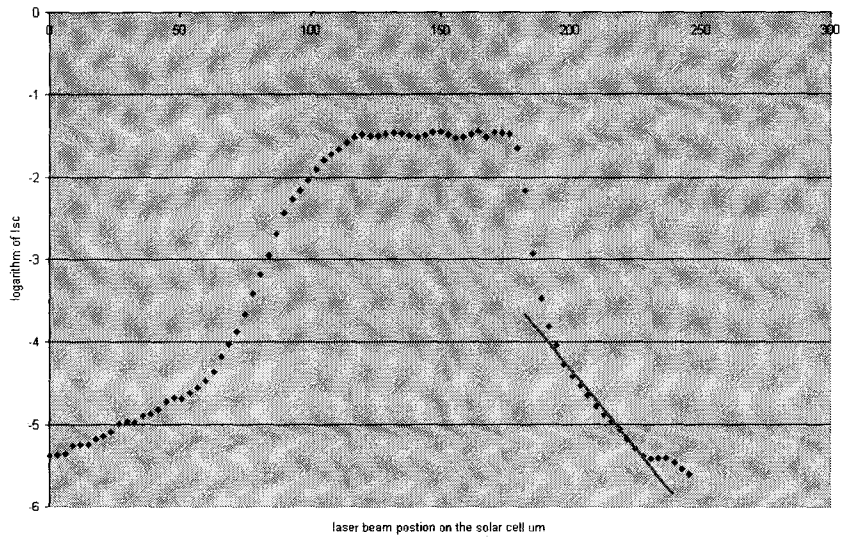


Figure 4.23: Logarithm of short-circuit current as a function of laser spot position for solar cell cut through

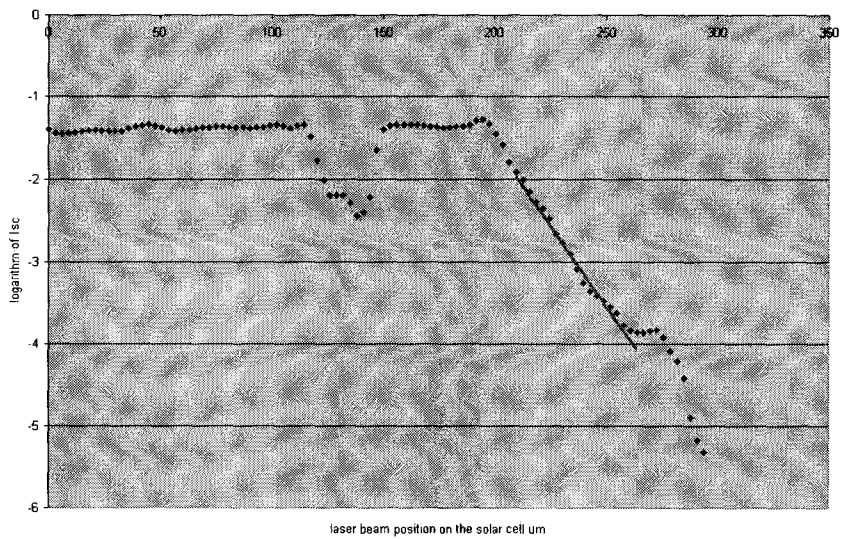


Figure 4.24: Logarithm of short-circuit current as a function of laser spot position for solar cell patriotically cut and then cleaved through

In fig.4.23, results of I_{sc} versus position are shown for a laser beam scanned across the junction from the top surface of a solar cell die which was diced all the way through. The flat region in this figure shows the top surface of the cell and then the declining part of the figure on the right side shows that the laser beam is scanning onto the junction. Since the laser beam moves 5 μm per step, the first 4 points in the junction are not considered in the diffusion length calculation. The straight line represents the linear relationship between the logarithm of the short circuit current and the laser spot position to the junction. The slope of this straight line characterizes the diffusion length of excess electrons in the p region the solar cell. The measured diffusion length from this solar cell die is 21.66 μm .

In fig. 4.24, a laser beam started scanning across the junction from the top surface of a solar cell which was diced partially and then cleaved through. The flat region in the figure describes the top surface of the cell and then the declining part of fig. 4.24 on the right side shows that the laser beam is scanning on the junction. The concave region on the flat part of the curve may be due to surface contamination which prevented the laser beam from fully illuminating the solar cell die surface. Applying the same measurement technique, the diffusion length of the excess electrons in the p region is 24.5 μm .

4.1.5 Correlation of three experiments

Three experiments were conducted to study what is the main reason for the efficiency loss.

In the storage delay time measurement the mean lifetimes of two solar cell die produced by different dicing methods were obtained by measuring the storage delay time. The corresponding diffusion lengths of excess electrons in the p region of the two types of solar cell die are also calculated. One diffusion length is $222\mu\text{m}$ and the other diffusion length is $110\mu\text{m}$. It would be expected that the cell with longer excess electron diffusion length will achieve a higher conversion efficiency. The result is consistent with the efficiency measurement. The partially diced cells possess a conversion efficiency of 15% which is higher than 8% for the fully diced cells. However, the diffusion lengths obtained by scanning a laser beam across the p-n junction of solar cell die give close diffusion length values (around $20\mu\text{m}$ to $30\mu\text{m}$) for both types of solar cell die. The large difference between the two experimental results reveals that the two measured diffusion lengths do not represent the same physical meaning; the diffusion length obtained by storage delay time measurement should be considered as the effective diffusion length which combines both the bulk part of the solar cell and the edge part of the cell. Meanwhile, the diffusion length obtained from the edge scanning experiment can only be used to describe the electron behavior of the near-edge region.

A light beam-induced current scanning experiment shows the surface maps of I_{sc} , V_{oc} , P_{max} for the two types of solar cell die by illuminating a $15\mu\text{m}$ laser beam on top of the solar cell die. Based on fig. 4.15 and 4.18, both types of cells show relatively constant surface maps of the three output parameters in the most of the inner surface. The dramatic transition of the three output values only takes place close to the edge region. Let us take I_{sc} to demonstrate the condition.

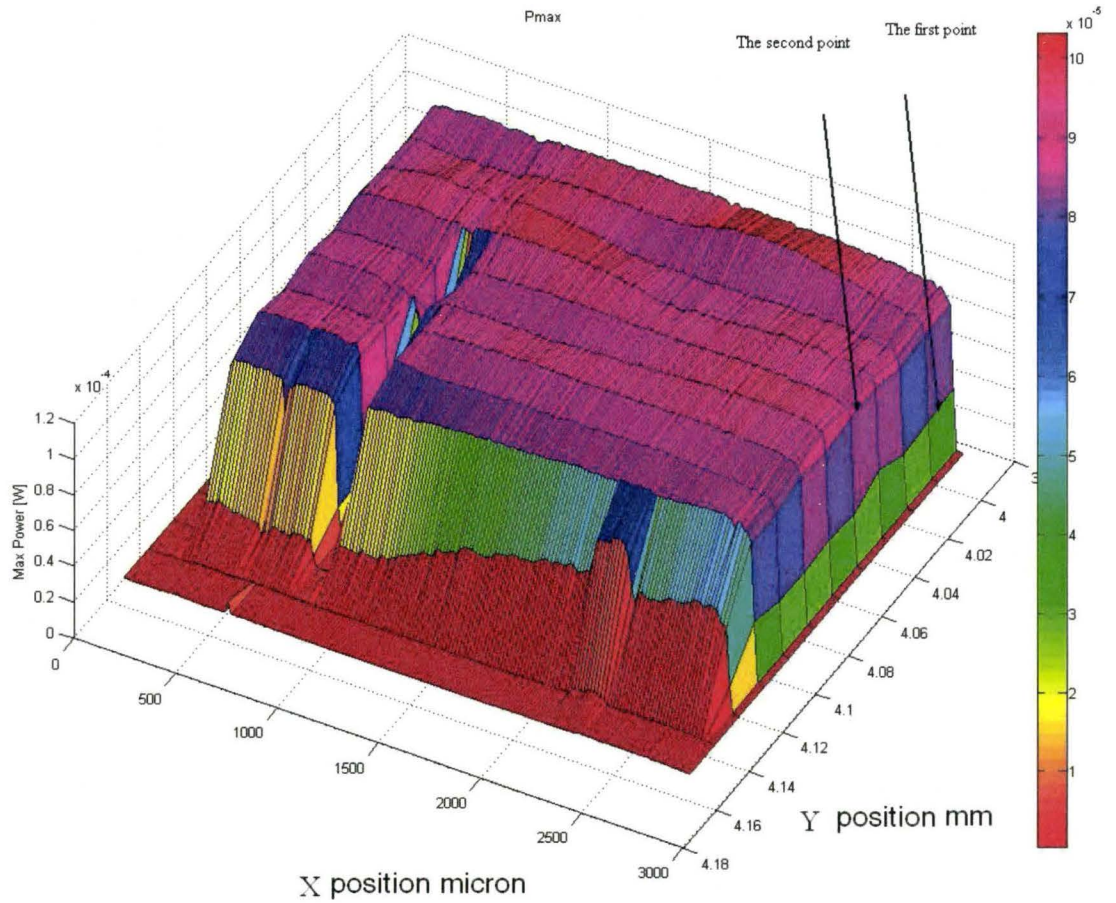


Figure 4.25: A diagram shows maximum output power at different location of the solar cell die surface

In fig.4.25, when the laser beam is scanning across the cell surface from right to left, at the first point on the right edge, the laser beam may not be fully on the cell; therefore, P_{max} is much lower than that of the inner regions. At the second point shown in fig.4.25, the laser beam is already fully illuminating inside the cell since the step between each scan is 20 μm which is larger than 15 μm of the laser beam diameter size. The observed P_{max} on the curve is still obviously lower than that of the inner cells. This tells that the damage near the edge may lower the maximum power in the vicinity of 40 μm from the edge. Beyond 40 μm , P_{max} does not show much variance. Within the region of 40 μm away from the edges, the excess electrons may have a diffusion length close to the value measured from the edge measurement, 30 μm . Beyond the 40 μm region from the edge, the excess electrons exhibit a diffusion length of the bulk part of the cell measured from the storage delay time measurement, 200 μm .

Most of the inner cell region shows good output parameters and are not affected by the edge damage. The efficiency difference rising from two dicing methods may be explained by the different degrees of increased shunt resistance around the edges. This proposition may be justified by measuring the slope of saturation currents in the third quadrant of the two types of cells in dark condition. The solar cells which were fully diced through exhibit a lower shunt resistance compared with the cell which were partially diced and then cleaved through. The shunt resistance is mainly due to the leakage of current from the edge of the cell. Fig.4.26 and 4.27 illustrate the reverse biased current of the two types of diced solar cells in the third quadrant. The I-V curves of fully diced chips and partially diced chips were traced in a dark condition.

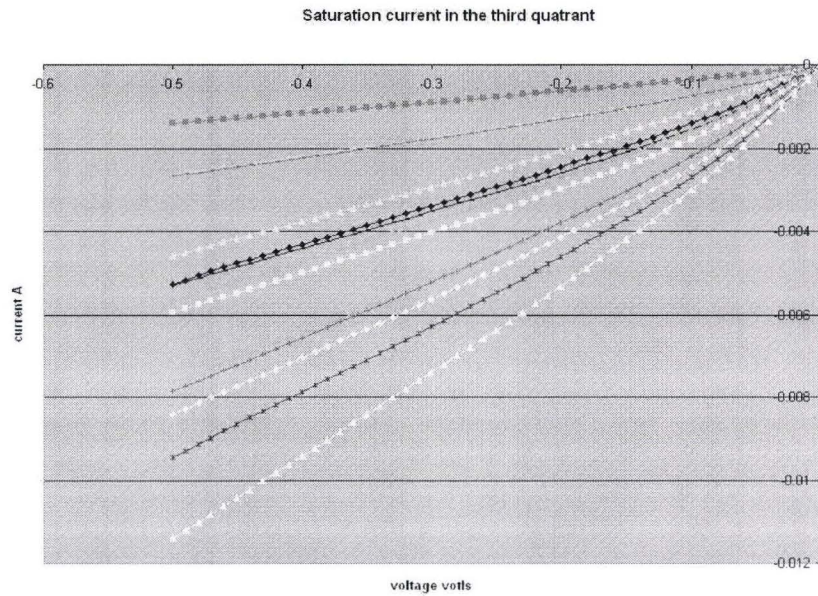


Figure 4.26: Saturation current of reverse biased solar cell die diced fully through

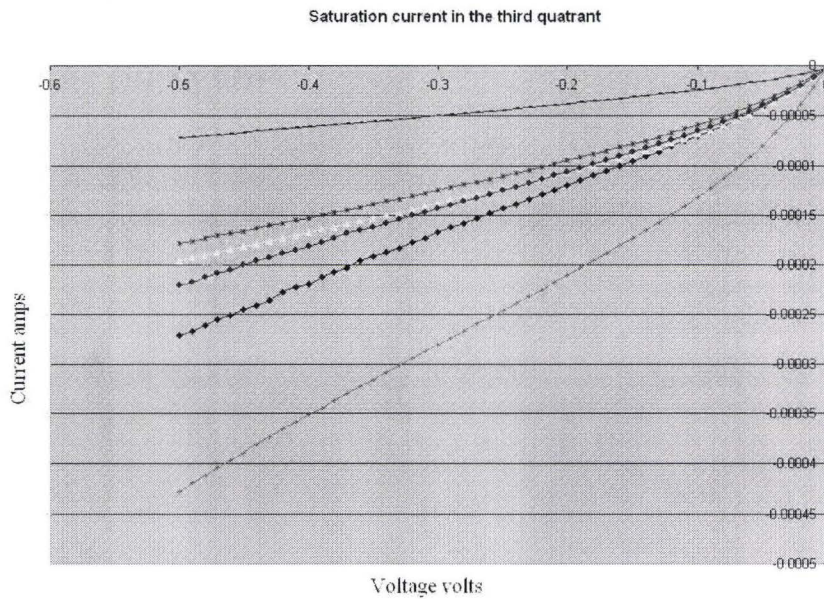


Figure 4.27: Saturation current of reverse biased solar cell die diced partially and cleaved through

The shunt resistance of each test cell can be estimated from the reciprocal of the slope of at each operating point of the I-V curve from equation:

$$R_{shunt} = \frac{V_i - V_{i-1}}{I_i - I_{i-1}} \tag{4.8}$$

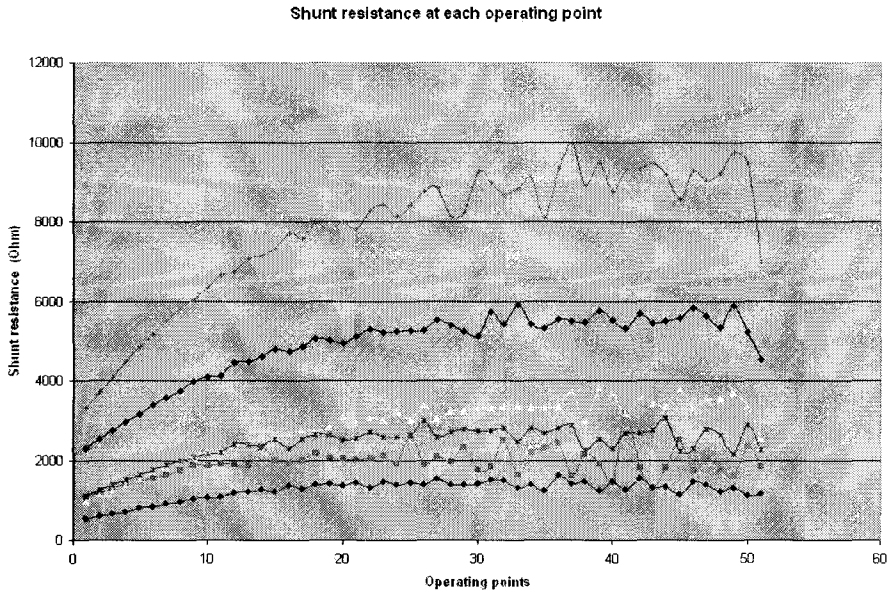


Figure 4.28: Shunt resistance at each operating point for cells which were partially diced and cleaved through

Equation 4.8 was applied to calculate the estimated shunt resistance at each operating point of the I-V curves of the test cells in the third quadrant. Fig.4.28 illustrates calculated shunt resistance for each operating point on the I-V curve in fig 4.27. Figure 4.28 illustrates that although the same type of diced cells show different reverse-biased saturation currents, the calculated shunt resistances of these diced cells are in the same order. The calculated shunt resistances are all in the order of one thousand ohms. Figure 4.29 shows shunt resistance in the order of one hundred ohms. The higher shunt resistance is, the less leakage current would shunt through the edges. Therefore, the cells which were partially diced and cleaved through will

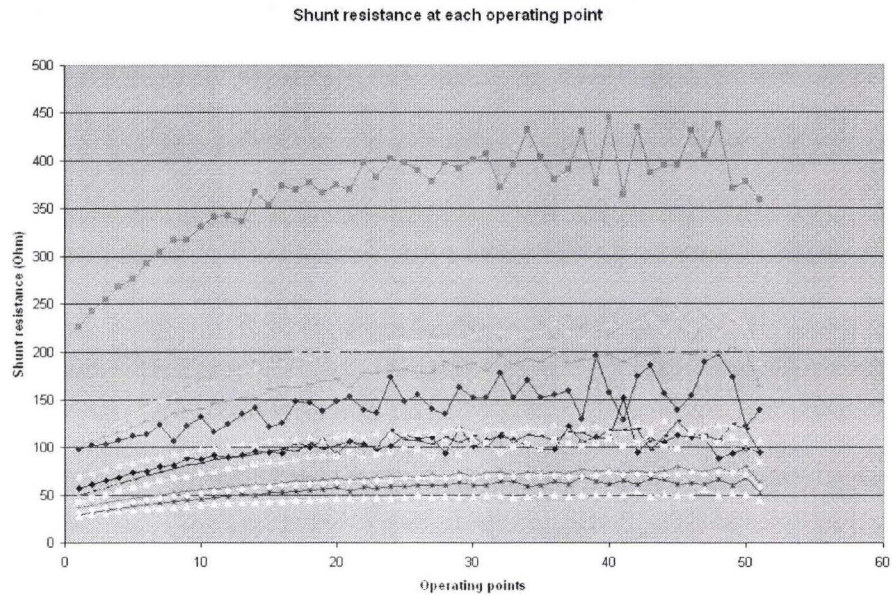


Figure 4.29: Shunt resistance at each operating point for fully diced cells

show better performance since less photo-generated current can pass through the edges from positive electrodes to negative electrodes.

4.2 Determination of angle dependence and lens spacing of solar cell performance

The goal of this experiment is to investigate the response of the output power of a solar cell to incident light at different angles so that a similar understanding of the output of a solar cell at different time during a bright day can be grasped.

Incident light of power 1000 W/m^2 is initially shining perpendicularly onto a 2.58 mm by 2.58 mm silicon solar cell die. The solar cell chip is mounted onto a rotational stage which can vary the light angle between the light source and the solar cell chip from 90 degrees to 0 degrees with ± 1 degree uncertainty as shown in fig. 4.30.

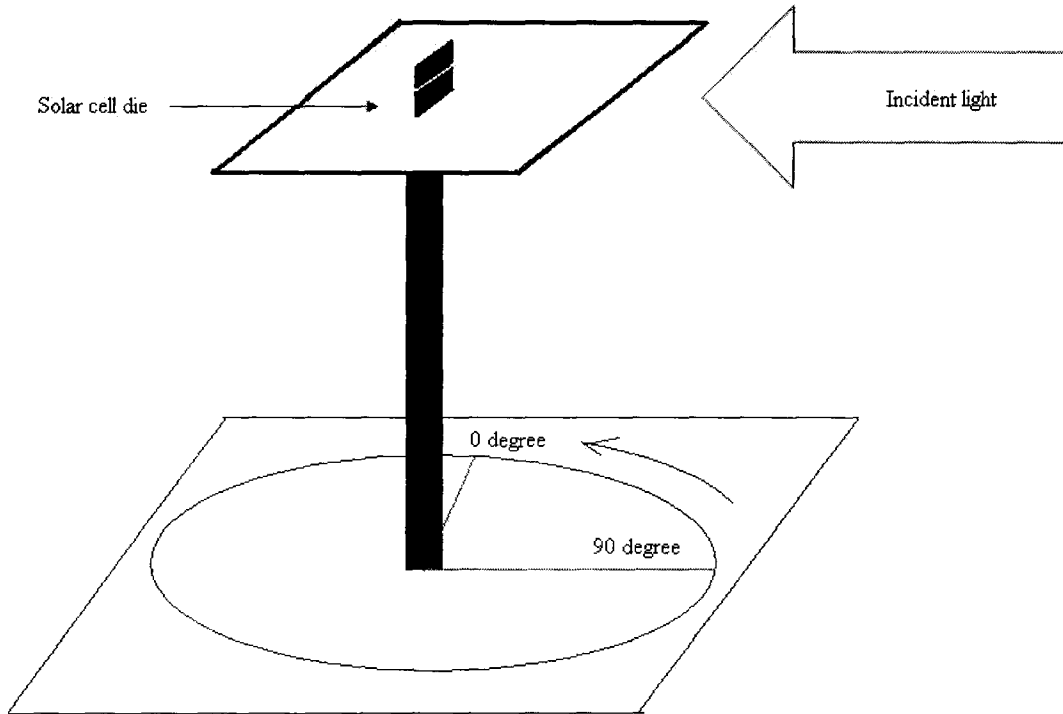


Figure 4.30: A schematic diagram of measurement of the determination of angle dependence of solar cell performance

I-V characteristics of the solar cell are measured through a Keithley current source unit 238 so that the traced IV curves of the solar cell die are compared at different angles. Another measurement was also conducted to investigate the effect of a lens on the power output of the solar cell die when a convex lens is mounted directly onto the solar cell die. Three main characteristics of a solar cell; short circuit current I_{sc} , open circuit voltage V_{oc} and maximum power P_{max} output are extracted from I-V curve data.

Theoretically, the trend line of the maximum power output versus angle is characterized by a Sine curve shape. For an incident light with an angle θ with the surface as shown in fig.4.31, the effective area to absorb all the incident light power is the product of area A and $\sin(\theta)$. When the light is perpendicular to the surface, the incident power onto the surface is the largest and equal to the light intensity times

area A . If the incident angle is 0, $\sin(0) = 0$, which means there is no light shining on the surface.

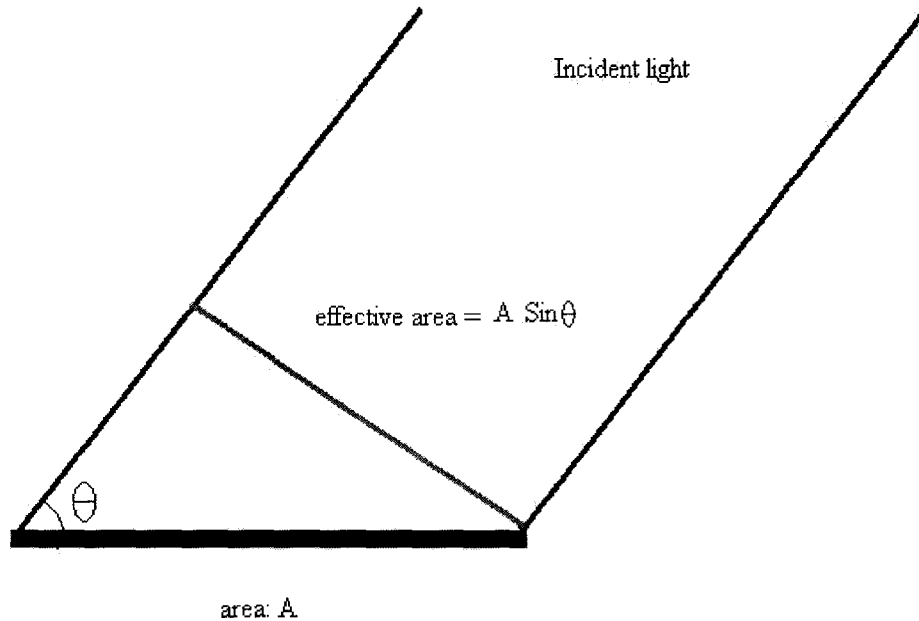


Figure 4.31: Effective absorption area of a surface when incident angle is θ

Assume the conversion efficiency of a solar cell at any light incident angle remains the same, the maximum output power should only depend on the incident angle. The varying angle experiment was conducted to verify the sinusoid relationship between the P_{max} and the varying angles. In the experiment, the angle between the solar cell die surface and the incident light varies from 90 to 0 degree with 10 degree steps between each measurement. Fig.4.32 compares the measured maximum power output P_{max} at each angle from the experiment data with a sinusoid curve. The blue curve represents the experiment data. When the incident light is perpendicular to the solar cell surface, measured P_{max} is at its largest. P_{max} decreases gradually from its maximum to zero when the incident angle is changed from 90 degrees to 0 degree. In the figure, the pink curve represents the theoretical sinusoidal relationship between the angle and maximum output power. After comparing the two curves, the

theoretical curve matches the experimental curve very well. The variation between the two may be due to the surface reflection of the incident light. The solar cell surface texture is designed to maximize the optical absorption of the incident light when the light is perpendicular to the surface. If the incident light is at a different angle other than the perpendicular incident angle, the light trapping would be less effective.

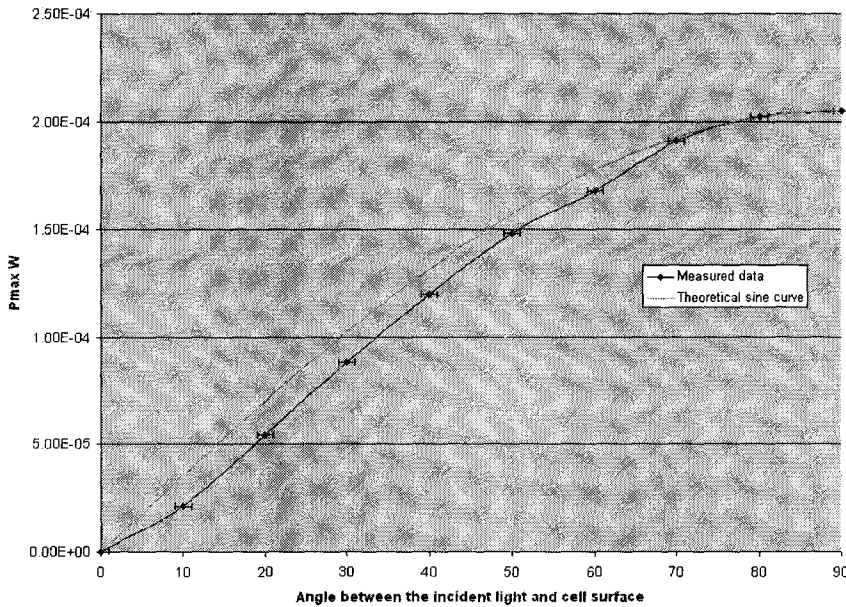


Figure 4.32: A comparison of a theoretical curve and measured data

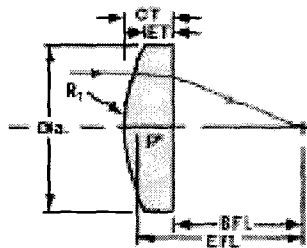


Figure 4.33: Parameters of a plano-convex lens [46]

A plano-convex lens is mounted in front of the surface of the solar cell die to demonstrate the effect of incorporation of a lens on a solar cell’s performance. A

Table 4.1: Plano-Convex Lens
[46]

Description	Dia. (mm)	E.F.L. (mm)	Back F.L. (mm)	C.T. (mm)	E.T. (mm)	Radius R1 (mm)	Glass
LENS PCX 4 × 4 UNCTD TS	4.0	4.0	3.06	1.70	1.00	3.21	LaSFN30

plano-convex lens from *EdmundOptics* was used and its description is listed in the table 4.1.

When a lens is mounted onto a solar cell, P_{max} is measured as θ is varied from 90 degree to 0 degree. A comparison of P_{max} with and without a lens is shown in figure 4.34.

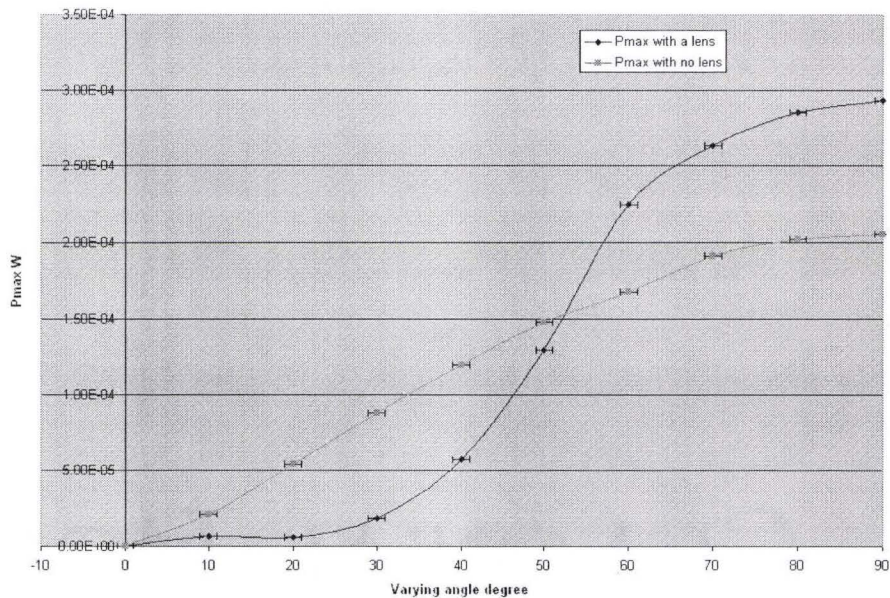


Figure 4.34: A comparison of P_{max} measurements with a lens and without a lens

Figure. 4.34 illustrates two measured P_{max} values at different conditions: one with a lens mounted on the solar cell and the other one without a lens mounted on the solar cell. At about 54 degrees between the incident light and solar cell surface, the P_{max} from each experiment are equal. For the graph, for $\theta < 54$ degrees, the

measured P_{max} with lens in front of a solar cell is greater than without a lens. After this point, the condition is the opposite. Integration of two curves over the angles gives us the total energy absorbed during the period of angle variation of the angle from 0 to 90 degrees. The ratio between two integrated energy is : E with lens /E without a lens = 1.039. At 90 degree when light is perpendicular to the cells surface, the ratio of P_{max} with and without a lens is 1.429.

Determination of focal properties

Simulation procedure

1. A parallel light source is initially normally shining onto a photo-detector and the corresponding detected power is obtained.
2. A convex lens is placed in front of the detector. The lens will focus the parallel light onto the detector. The distance between the lens and the detector to be investigated are 0mm, 0.5mm, 1mm and 1.5mm.
3. For each spacing, the incident light angles are changed from 90 degrees to 0 degree and P_{max} at different angles are recorded from the detector.
4. Graph curves of different spacings.
5. Integrate area under each curve from 0 degrees to 90 degrees to obtain energy.

* note: the integral value for 0 spacing is normalized to 1 and other values are normalized relative to the integral of 0mm spacing.

Table 4.2: Integration comparison

Distance between the lens and the detector	Integral ratio*
0 mm	1
0.5 mm	99.33%
1 mm	85.39 %
1.5 mm	73.04%
No lens	84.23%

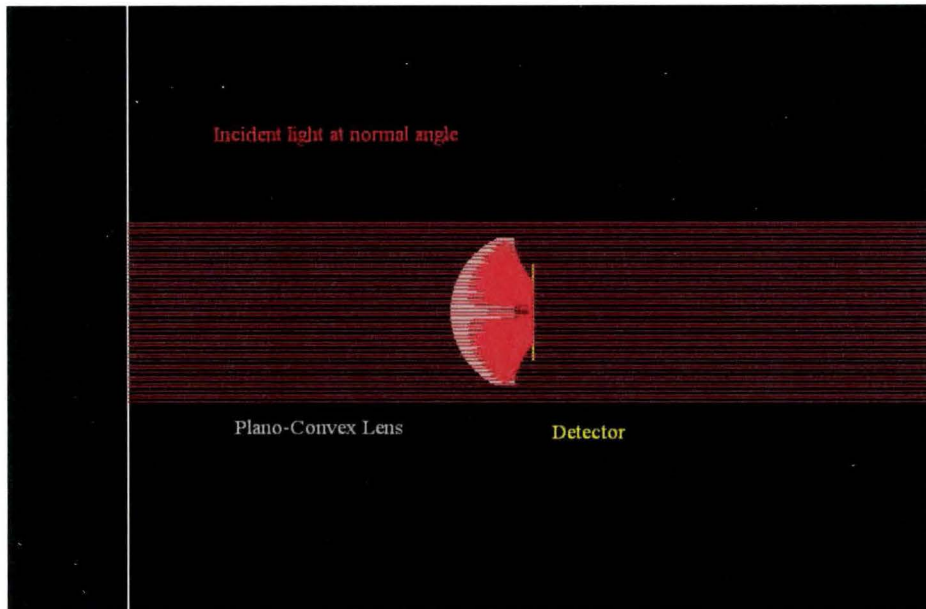


Figure 4.35: A simulation using OpticsLab software

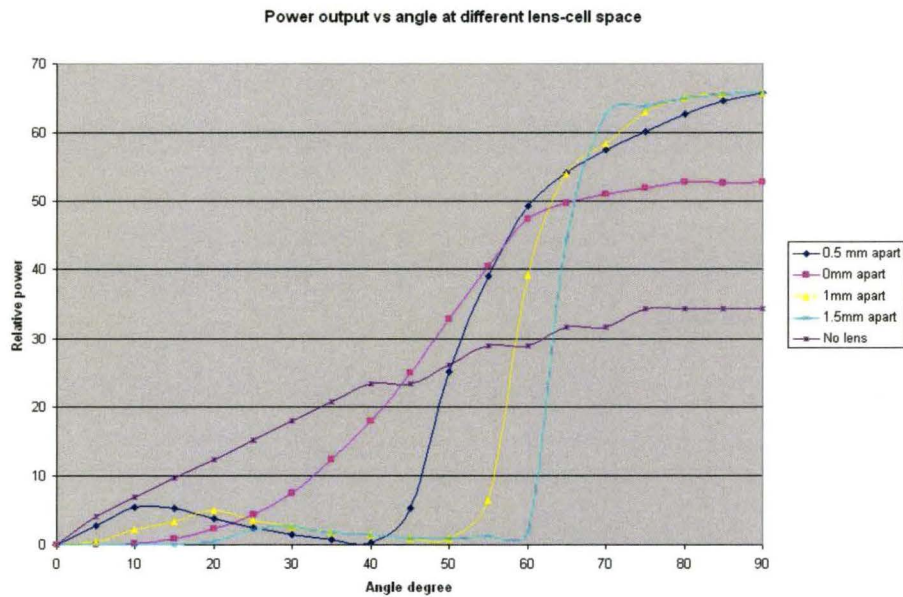


Figure 4.36: Power output vs angle at different lens-cell space

Table 4.2 compares the energy integration of incident angles from zero degrees to ninety degree for different lens spacings.

The goal is to investigate the effect of distance between a lens and a solar cell chip on P_{max} output. The simulation helps to understand the change of the total absorbed energy due to different distances between a lens and a solar cell. An optimized distance is extracted from this simulation and then will be used to set spacing between a lens and a solar cell die. An optical software, OpticsLab version 4.26, was used to simulate the relationship of maximum output power, and the distance between the solar cell and a lens. All the parameters of the lens in the software are defined to match the parameters of the lens from EdmundOptics as listed in table 4.1. A detector was used to replace the solar cell in the simulation. Fig. 4.35 shows that light is perpendicularly incident onto a detector covered by a lens. In fig.4.36, five different curves show five different cell-lens spacings. The simulated power-angle relations for cell-lens spacing at 0.5mm, 1mm and 1.5mm show an unexpected increase after the power has decreased to zero. The reason the power for these three curves first falls to zero as the angle decreases is because the light is focused away from the cell surface. A subsequent power increase starts at about 60 degrees, 50 degrees and 40 degrees for cell-lens spacing at 1.5mm, 1mm and 0.5mm respectively. This is due to the fact that some portion of the light directly hits the solar cell without passing through the lens. As angle further decreases along the horizontal axis in the fig.4.36, the power will become zero again when the incident light is parallel with the cell surface.

A conclusion can be drawn from table 4.2 is that the maximum power can be delivered out of the detector when the spacing between the lens and the detector is 0mm.

Chapter 5

Conclusion

The technology being developed is a flexible solar panel using small silicon solar cell die arranged in arrays. All die are connected together to allow the chip outputs to combine to produce a flexible solar panel. Since the approach is based on well-known bulk silicon technology, the result is unique: the concept enables high conversion efficiency and long term stability (over 25 years continuous service) in a package that is flexible, lightweight and thin, rather than the glass-encapsulated silicon cells usually associated with this type of performance.

A comparison of effects of two dicing processes on the electrical performance of solar cells have been conducted. The result shows that the solar cell which is diced completely through has a lower conversion efficiency (around 8 %) than that of solar cell diced partially and then cleaved through manually (around 14%). This result is investigated through three different experiments.

First, in the storage delay time measurement, the lifetime of excess electrons in the p region of solar cell die (2.58 mm by 2.58 mm) was calculated from the measured delay time of the stored excess carriers in the p region by applying AC current through the solar cell die. The measured data show that the solar cell die which was diced completely through gives a lifetime of $3.04\mu\text{s}$ and the solar cell which was diced partially and then cleaved through gives a lifetime of $12.39\mu\text{s}$. The measured lifetime is an effective lifetime of the bulk part of the solar cell and the surface part of the solar cell. The corresponding diffusion length of excess electrons for these two

lifetime values are $110\ \mu\text{m}$ and $220\ \mu\text{m}$ for respective dicing processes. This result is consistent with the direct efficiency measurement: longer diffusion length indicates higher conversion efficiency.

Second, light beam induced current (LBIC) scanning was employed by using a focused laser beam to probe a small area (beam diameter is about $15\ \mu\text{m}$) on a solar cell to investigate the local characteristics, especially the performance of a solar cell near the edge region. It is found out that the region about $40\ \mu\text{m}$ away from the edge shows uniform and higher performance in terms of short circuit current, open circuit voltage and maximum output power. These three parameters are much lower values within $40\ \mu\text{m}$ from the edges of a diced solar cell. Solar cells diced by two dicing processes show similar spatial response of these three important parameters.

Third, traveling light spot diffusion length measurement was used to determine the diffusion length of excess electrons at p region near the diced edge surface. It is expected that the surface electron-hole recombination at the diced edge is much higher than that of the bulk part of a solar cell since the damage caused by the dicing process introduces a large number of defects, such as dangling bonds at the edges as recombination centers. The measured diffusion lengths for the partially-diced-through cells and the fully-through cells are all around $20\ \mu\text{m}$ and $30\ \mu\text{m}$. This low diffusion length at the surface indicates the large influence of surface recombination and rough surface condition on the diffusion length measurement. However, since both types of cells show similar surface recombination, the explanation for different diffusion efficiencies by different dicing processes may be not the recombination at the edge surface.

It is proposed that different shunt resistances introduced by two dicing processes causes the large deviation of conversion efficiencies. An ideal solar cell will have infinitely large shunt resistance since there will be no current shunt through the cell.

Therefore, the larger the shunt resistance is, the better performance will be for a solar cell. The shunt resistance of two types of diced solar cells were measured from IV curves when they were reversed biased in a dark condition. It is observed that the cells diced completely through show deeper slopes of IV curves on average when reverse biased. This indicates that they have smaller shunt resistance. The cells diced partially through show larger shunt resistance on average.

Therefore, the conclusion is that the large efficiency difference between two types of diced cells results from different shunt resistances given to them by their respective dicing processes. The solar cell that is diced partially and then cleaved through shows a lower efficiency loss since there is less photo-generated current shunt through the solar cell.

Incident light angle and lens spacing dependence were also studied to simulate the response of a lensed solar cell during the day time. Solar cells show a Sine output power dependence at varying angles. The simulation of output power versus lens spacing indicates that when a solar cell touching a lens it offers the largest overall energy output if the energy is integrated from a zero degree incident angle to a ninety degree incident angle.

Chapter 6

Future work

The structure of the flexible silicon solar cell fabricated for this thesis is achieved by interconnecting arrays of silicon solar cell die. However, the space between solar cell die is filled by epoxy material. Sunlight that enters the solar cell may fall between the silicon cell die in which case this portion of light does not generate electrical power. This situation may be resolved by deflecting this sunlight onto the nearest silicon chip. The result may be accomplished with a novel non-spherical Surlyn lens that deflects light onto the silicon chips, without preventing sunlight entering at an angle from generating power during off-peak times of the day. The approximate shape of the lens is illustrated in figure.6.1

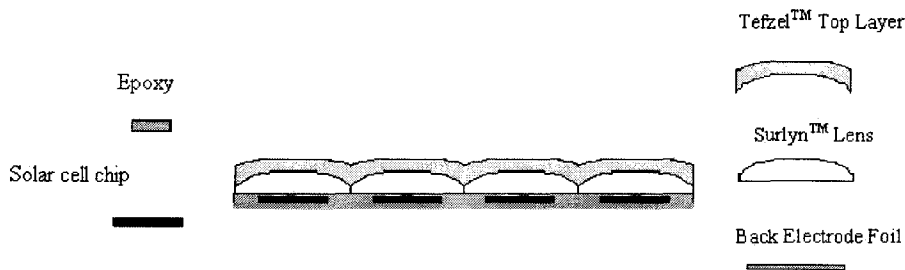


Figure 6.1: Schematic diagram showing cross section view of the structure and components of a flexible silicon solar cell

The use of Surlyn lensing reduces the total amount of silicon needed to achieve a given electrical power rating for the solar cell by 20-40%.

Since the solar cell die are cut from commercial silicon solar cells, there will be inevitable loss due to the dicing process. One ultimate way to resolve this efficiency

loss is to fabricate the same size of solar cell from silicon casting methods by filling a mold with purified silicon liquid. The molded silicon die will be doped to create p-n junction structure. Front and back contacts will also be added into the structure. Finally, the molded solar cells will be directly incorporated into the flexible solar cell structure to replace the current diced solar cell die.

Bibliography

- [1] A.E.Becquerel, Comt Rend. Academie d. Sciences **9**, 561 (1839).
- [2] R.Williams, The Journal of Chemical Physics. **32**, 5 (1960).
- [3] J.Nelson, *The Physics of Solar Cells* (Imperial College Press, London, 2003).
- [4] C. D.M.Chapin and G.L.Pearson, J.Appl.Phys. **25**, 676 (1956).
- [5] P.A.LLes and F.Ho, Conference Record of the IEEE Photovoltaic Specialists Conference **2**, 1957 (1994).
- [6] M. S.Pizzini and S.Binetti, Phys.Stat.Sol. **202**, 2928 (2005).
- [7] M.A.Green, *High Efficiency Silicon Solar Cells* (Trans Tech Publications, Aedermansdorf, 1987).
- [8] M.A.Green, Progress in Photovoltaics: Research and Applications. **14**, 455 (2006).
- [9] L.L.Kazmerski, Renewable & Sustainable Energy Reviews **1**, 71 (1997).
- [10] A.Goetzberger and V.U.Hoffmann, *Photovoltaic Solar Energy Generation* (Springer, New York, 2005).
- [11] R. W.O'Mara and L.Hunt, *Handbook of Semiconductor Silicon Technology* (Noyes Publication, Park Ridge, 1990).
- [12] R.M.Moore, Solar Cells **86**, 1627 (1981).
- [13] T. T.F.Coszek, M.R.Page and J.A.Casey, Conference Record of the IEEE Photovoltaic Specialists Conference (2002).

- [14] T.Markvart and L.Castaner, *Practical Handbook of Photovoltaics: Fundamentals and Applications* (Elsevier Science Inc, New York, 2003).
- [15] A. R.L.Wallace, J.I.Hanoka and G.Crotty, *Solar Energy Materials & Solar Cells* **48**, 179 (1997).
- [16] E.Bucher, *Physics in Technology* **17**, 152 (1986).
- [17] J. D. R. K.D.Smith, H.K.Gummel and W.Rosenzweig, *Bell Syst.Tech.J.* **41**, 1765 (1963).
- [18] J.Lindmayer and J.Allison, *Solar Cells* **3**, 1 (1973).
- [19] R. J.Haynos, J.Allison and A.Meulenber, *Int.Conf.on Photovoltaic Power Generation* (1974).
- [20] R. R.R.King and R.M.Swanson, *Conference Record of the IEEE Photovoltaic Specialists Conference* **1**, 538 (1988).
- [21] J.Mandelkorn and J.H.Lamneck, *J.Appl.Phys.* **44**, 4785 (1973).
- [22] A. J.Zhao and M.A.Green, *Solar Energy Materials & Solar Cells* **65**, 429 (2001).
- [23] J.Kim, *Science* **317**, 5835 (2007).
- [24] Y.Hamakawa, *Thin-Film Solar Cells* (Springer-Verlag, Berlin, 2004).
- [25] D.E.Carlson and C.R.Wronski, *Appl.Phys.Lett.* **28**, 671 (1976).
- [26] A.E.Becquerel, *Appl.Phys.Lett.* **31**, 292 (1977).
- [27] S. J.Yang and A.Banerjee, *Materials Research Society Symposium - Proceedings* **467**, 693 (1997).
- [28] M.Izu and T.Ellison, *Solar Energy Materials & Solar Cells* **78**, 613 (2003).
- [29] D. G.G.Wallace, P.C.Dastoor and C.O.Too, *Chemical Innovation* **30**, 15 (2000).
- [30] N. C.J.Brabec and J.C.Hummelen, *Advanced Functional Materials* **11**, 15 (2001).

- [31] S.M.Sze, *Physics of Semiconductor Devices* (John Wiley & Sons, Toronto, 1969).
- [32] J. F.A.Lindholm and E.L.Burgess, *IEEE Transactions on Electron Devices* **ED-26**, 165 (1979).
- [33] B.Streetman and S.K.Banerjee, *Solid State Electronic Devices* (Pearson Education Inc., New Jersey, 2006).
- [34] G.Jungk and H.Menniger, *Phys.Stat.Sol.* **5**, 169 (1964).
- [35] R. J.E.Mahan, T.W.Ekstedt and R.Kaplow, *IEEE Transactions on Electron Devices* **ED-26**, 733 (1979).
- [36] V.K.S.Ong, *Review of Scientific Instruments* **69**, 1814 (1998).
- [37] J.R.Hauser and P.M.Dunbar, *IEEE Transactions on Electron Devices* **ED-24**, 305 (1977).
- [38] F.Guibaly and K.Colbow, *J.Appl.Phys.* **52**, 5247 (1981).
- [39] F.A.Lindholm and C.Sah, *IEEE Transactions on Electron Devices* **ED-24**, 299 (1977).
- [40] W.Shockley, *Bell Syst.Tech.J.* **28**, 435 (1949).
- [41] A. D. H.O.Jacobs, A.R.Tao and G.M.Whitesides, *Science* **296**, 323 (2002).
- [42] *Natl.Bur.Stand.(U.S.), Monogr.* **25**, 13 (1976).
- [43] V. V. Vlack, *Elements of Materials Science and Engineering*, 6th ed. (Addision Wesley, New York, 1989).
- [44] F.J.Vorster and E.E.V.Dyk, *Review of Scientific Instruments* **78**, 01394 (2007).
- [45] F.J.Vorster and E.E.V.Dyk, *Solar Energy Materials & Solar Cells* **91**, 871 (2007).
- [46] <http://www.edmundoptics.com/onlinecatalog/displayproduct.cfm?productID=1747&search=1>, .